UNCLASSIFIED

AD NUMBER
ADB274269
NEW LIMITATION CHANGE
TO Approved for public release, distribution unlimited
FROM Distribution authorized to U.S. Gov't. agencies only; Proprietary Info.; Jul 2001. Other requests shall be referred to U.S. Army Medical Research and Materiel Command, 504 Scott St., Ft. Detrick, MD 21702-5012.
AUTHORITY
USAMRC Ltr, 26 Aug 2002

THIS PAGE IS UNCLASSIFIED

AD_____

Award Number: DAMD17-98-1-8148

TITLE: Development of Quantitative Microvascular Breast MRI

PRINCIPAL INVESTIGATOR: Brian Rutt, Ph.D.

CONTRACTING ORGANIZATION: John P. Robarts Research Institute
London, Ontario, Canada N6A 5K8

REPORT DATE: July 2001

TYPE OF REPORT: Final

PREPARED FOR: U.S. Army Medical Research and Materiel Command
Fort Detrick, Maryland 21702-5012

The views, opinions and/or findings contained in this report are
those of the author(s) and should not be construed as an official
Department of the Army position, policy or decision unless so
designated by other documentation.

20020117 050

NOTICE

THIS TECHNICAL REPORT HAS BEEN REVIEWED AND IS APPROVED FOR PUBLICATION.

_____   _01/04/02_____

REPORT DOCUMENTATION PAGE		Form Approved OMB No. 074-0188

Public reporting burden for this collection of information is estimated to average 1 hour per response, including the time for reviewing instructions, searching existing data sources, gathering and maintaining the data needed, and completing and reviewing this collection of information. Send comments regarding this burden estimate or any other aspect of this collection of information, including suggestions for reducing this burden to Washington Headquarters Services, Directorate for Information Operations and Reports, 1215 Jefferson Davis Highway, Suite 1204, Arlington, VA 22202-4302, and to the Office of Management and Budget, Paperwork Reduction Project (0704-0188), Washington, DC 20503

1. AGENCY USE ONLY (Leave blank) •	2. REPORT DATE July 2001	3. REPORT TYPE AND DATES COVERED Final (1 Jul 98 – 30 Jun 01)	
4. TITLE AND SUBTITLE Development of Quantitative Microvascular Breast MRI			**5. FUNDING NUMBERS** DAMD17-98-1-8148
6. AUTHOR(S) Brian Rutt, Ph.D.			

7. PERFORMING ORGANIZATION NAME(S) AND ADDRESS(ES) John P. Robarts Research Institute London, Ontario, Canada N6A 5K8 E-Mail: brutt@irus.rri.on.ca	8. PERFORMING ORGANIZATION REPORT NUMBER

9. SPONSORING / MONITORING AGENCY NAME(S) AND ADDRESS(ES) U.S. Army Medical Research and Materiel Command Fort Detrick, Maryland 21702-5012	10. SPONSORING / MONITORING AGENCY REPORT NUMBER

11. SUPPLEMENTARY NOTES

12a. DISTRIBUTION / AVAILABILITY STATEMENT Distribution authorized to U.S. Government agencies only (proprietary information, Jul 01). Other requests for this document shall be referred to U.S. Army Medical Research and Materiel Command, 504 Scott Street, Fort Detrick, Maryland 21702-5012.	12b. DISTRIBUTION CODE

13. ABSTRACT (Maximum 200 Words)

The purpose of this research is to develop a non-invasive predictor of malignancy in breast tumours through the design and preliminary validation of a new form of magnetic resonance imaging (MRI). The hypothesis is that the spatial distribution of microvasculature around a solid breast lesion is specific for malignancy and can be reliably measured at high resolution by a completely non-invasive, non-contrast-enhanced MRI method. This is being tested by achieving the following:
1. Design/building/testing of ultra-high-strength gradient coils for human breast imaging at 1.5 Tesla (T) and 4T.
2. Design/implementation/testing of MR pulse sequences for selective mapping of microvascular parameters.
3. Correlation of MR-derived microvascular parameters with true microvessel density in a rat model of human breast cancer.

A gradient coil has been designed that is suitable for high resolution imaging of tumours in rats and achieves gradient strengths up to 300mT/m (typical clinical systems achieve 40mT/m). A non-contrast-enhanced MRI pulse sequence that uses diffusion weighting has been implemented at 1.5T, and has been used to acquire images of breast tumours in rats. Using an analysis program designed in house, our results show that our technique allows imaging of the micravasculature in tumours.

The significance of this research is that, with relatively low-cost modifications to MR imaging equipment, it should be possible to detect, diagnose, and provide much improved prognosis of lesions suspected to be breast cancer. Further, this technique will measure non-invasively the microvasculature, allowing monitoring of anti-angiogenic treatments.

14. SUBJECT TERMS Breast Cancer, tumour, angiogenesis, microvessel density, high strength gradient coils, high field MRI diagnosis			15. NUMBER OF PAGES 47
			16. PRICE CODE

17. SECURITY CLASSIFICATION OF REPORT Unclassified	18. SECURITY CLASSIFICATION OF THIS PAGE Unclassified	19. SECURITY CLASSIFICATION OF ABSTRACT Unclassified	20. LIMITATION OF ABSTRACT Unlimited

Table of Contents

Introduction

X-ray mammography is currently the clinically accepted modality for breast cancer screening. Mammography, however, is particularly unreliable and recent trials have shown that 70-80% of mammographically indeterminate lesions that progress to surgical biopsy are benign.[1-4] Development of an accurate, non-invasive imaging test with low false negative rates would allow reduction of the two step process of surgical biopsy followed by surgical lesion removal to a single step, as well as providing a tool for guiding treatment decisions. It may be possible to achieve this through the development of a non-invasive technique that measures microvessel density. Tumour progression is known to be dependent on the ability to stimulate the growth of new blood vessels that supply nutrients and oxygen to the expanding tumour. Based on recent studies that indicate that the onset of angiogenesis can occur before a tumour reaches its maximum diffusion-limited growth potential (1-2 mm diameter) and may occur well before the switch to a malignant phenotype,[5-15] it has been hypothesized that the characteristic new vessel growth associated with tumour angiogenesis should allow differentiation between malignant and benign breast lesions.[16-21] The purpose of this research is to develop a non-invasive predictor of malignancy through the design and preliminary validation of a new form of magnetic resonance imaging (MRI) called the IntraVoxel Incoherent Motion (IVIM) method which utilises high main magnetic field strength and ultra-strong magnetic field gradients. This technology will permit completely non-invasive, quantitative characterization of tumour microvasculature at high spatial resolution over the entire breast.

Body

Hardware Development

A high strength gradient coil has been designed. The prototype coil was built with an inner diameter of 5 cm, which is ideal for mice. A second coil has now been built that is more suitable for rats. This coil has an inner diameter of 24 cm, which can accommodate a rat plus the equipment used to monitor the animal. The maximum gradient strength achievable with this coil is 300 mT/m, which is almost ten times greater than typical clinical systems and is sufficient for the high-resolution imaging experiments proposed in this grant. Testing of the coil on a 1.5 Tesla (T) clinical MRI system is nearly completed. It was found that wire density and power dissipation considerations required that the coil be constructed in a multilayer configuration. Details regarding the design and construction of the coil are given in the paper[27] in Appendix I.

Pulse Sequence Development

An IVIM pulse sequence has been designed based on a standard diffusion-weighted imaging sequence. The sequence consists of a spin echo, echo planar imaging sequence with the addition of strong magnetic field gradients that cause the contrast in the images to be weighted based on the diffusion of water in the microvascular and extra-vascular compartments. We have incorporated a phase correction method that allows post-acquisition correction of the images for small-scale motion of the object being imaged.

A computer program has been written in an interactive windows environment that allows analysis of the diffusion-weighted images obtained with the IVIM pulse sequence. The program allows calculation of the diffusion coefficients either for each pixel in the images, or for the average values in a region of interest. Validation of the program has been performed using simulated data. Further validation of both the program and the IVIM sequence has been performed using phantoms that are spherical containers filled with water and acetone. The results obtained (see Appendix II) agree well with those found in the literature.

Validation of Microvascular Imaging

A tumour model has been implemented in rats using N-ethyl-N-nitrosourea (ENU). ENU is known to be a potent carcinogen that induces well vascularised mammary tumours in rats.[22] This tumour model was chosen because a range of benign and malignant tumours develop depending on the dose of ENU administered and because the tumour morphology and angiogenic behavior closely mimic breast tumours in humans. Tumours have been successfully grown in rats using both high dose and low dose injections of ENU. IVIM images of the tumours have been obtained for each rat. High signal to noise ratios (SNR) are required in the images in order to observe the microvascular component of the measured signal. The mean SNR in the images of the tumours was 392 ± 126, which was sufficient for this study.

Seven rats were sacrificed immediately after imaging of the tumour, and imaging was repeated on the sacrificed animal. The diffusion decay curves obtained pre-sacrifice were not mono-exponential, but rather, were at least bi-exponential. Sample decay curves for one tumour showing the diffusion decay pre- and post-sacrifice are shown in Appendix III, Figure 1. The magnitude of the diffusion coefficient corresponding to the fast decay in the pre-sacrifice curves was on the order of that expected for the microvascular blood flow. Post-sacrifice, the fast decay component disappeared, but the curves were not mono-exponential as was expected. An intermediate diffusion coefficient, or a diffusion rate intermediate to the pre-sacrifice low and high rates, was present post-sacrifice. A plot of the two diffusion coefficients versus the fractional volumes contributing to the coefficients for each of the seven tumours pre- and post-sacrifice is shown in Appendix III, Figure 2. These results suggested that while the fast decay component appears to be related to the flow of blood in the microvasculature, a third diffusion rate may be present.

Initially, the diffusion decay curves were acquired to a maximum b-value of 1000 s/mm². In order to determine if a third diffusion rate was present, diffusion decay curves were acquired to a maximum b-value of 5000 s/mm². The decay curves were fit using a linear non-negative least squares (NNLS) fitting algorithm. This algorithm does not require *a priori* knowledge of the number of components present in the decay curve, but rather chooses the number of components that best fits the data. A plot of the

6

diffusion coefficients versus the fractional volumes contributing to the coefficients obtained using the NNLS algorithm for four tumours pre- and post-sacrifice is shown in Appendix III, Figure 3. The NNLS algorithm found three distinct diffusion decay coefficients in three of the four pre-sacrifice decay curves. In one presacrifice curve, only the low and intermediate diffusion coefficients were present. In all four post-sacrifice curves, only two coefficients were found – the low and intermediate values. The absence of the high diffusion coefficient in the post-sacrifice decay curves suggest that the high diffusion rate is due to the flow of blood in the microvasculature and that the IVIM method is capable of measuring the tumour microvasculature. Decay curves extending to a maximum of 5000 s/mm^2 have been collected from additional tumours, and analysis of this data is underway.

The tumours used in this study have been resected and pathology is currently being performed on each tumour to determine the degree of malignancy and the density of microvessels in the tumours. The pathological results will be correlated with the diffusion coefficients.

Key Research Accomplishments

- Design of a mouse-sized gradient coil with gradient strengths that exceed 2000 mT/m. (Approximately 50 to 100 times higher than typical clinical MRI systems.)

- Design and construction of a gradient coil with an inner diameter of 24 cm, which is large enough to accommodate a rat and animal monitoring equipment. Maximum gradient strengths achieved with this coil are 300 mT/m.

- Implementation of a fast IVIM pulse sequence that allows acquisition of diffusion weighted images with high signal to noise.

- Design and coding of a computer program that allows automated analysis of the diffusion weighted images for the calculation of diffusion coefficients.

- Validation of the MR pulse sequence analysis program using simulated data and images acquired from substances with known diffusion coefficients.

- Implementation of a breast tumour model in rats that produces tumours with a range of malignancies from benign to malignant.

- Acquisition of high signal to noise ratio, *in vivo*, diffusion weighted images of tumours in the rats using the IVIM method.

- Verification of three unique diffusion rates in the pre-sacrifice tumours.

- Verification that the highest diffusion rate is related to the flow of blood in the microvasculature.

Reportable Outcomes

Presentations and Publications

1. The design and construction of the gradient coils resulted in three peer-reviewed publications[23,24,27] and two conference presentations.[25,26] These three publications are appended (Appendices I, IV, and V).

2. The preliminary results of the acquisition and analysis of the images acquired from the animal tumour model were presented at the Era of Hope Meeting, Atlanta, June 8-12, 2000.

At least two additional papers are planned for submission after the analysis of the decay curves and the pathology of the resected tumours has been completed. It is projected that these papers will be submitted before the end of this year (2001).

Funding

Two post-doctoral fellowships were awarded to perform the research supported by this grant:

1. To Dr. Paula Gareau by the Department of Defense Breast Cancer Research Program of the United States Army Medical Research and Materiel Command. Grant Number BC980729.

2. To Dr. Lanette Friesen-Waldner by the Natural Sciences and Engineering Research Council of Canada.

Dr. Lanette Friesen-Waldner was recently awarded a postdoctoral traineeship from the Department of Defense U.S. Army Medical Research and Materiel Command's 2000 Breast Cancer Research Program. Grand Number BC000657. The research proposed in this traineeship is based on the work outlined in this report.

Conclusions

We designed a mouse-sized gradient coil and a gradient coil large enough to accommodate rats and animal monitoring equipment. Both coils achieve gradient strengths significantly higher than typical clinical MRI systems. Based on wire density and power dissipation considerations, we concluded that small coils with high gradient strengths, such as those required for high resolution IVIM imaging, require multi-layer configurations. The design for the coils constructed here should be scalable to a breast-sized coil. Such a coil will allow imaging of the human breast at resolutions that, until now, have been unattainable, thus allowing visualisation of very small lesions within the breast.

The IVIM pulse sequence was implemented on our 1.5T clinical MRI system. We are able to acquire IVIM images with high signal to noise ratios (at least 200). A computer program was written to analyse the IVIM images. The pulse sequence and analysis program were validated using substances with known diffusion coefficients.

An animal tumour model was implemented, and IVIM images of the tumours were acquired. We have shown that three diffusion rates exist in the tumours and that, in order to properly separate and accurately classify all three components, the diffusion decay curve must be sampled to a maximum b-value of at least 5000 s/mm^2. A multi-exponential fitting algorithm, such as NNLS, capable of more than bi-exponential fitting, must be used to determine accurately the diffusion coefficients from the decay curves. The largest of the three diffusion rates detected by the IVIM method is absent after cessation of blood flow. For this reason, we believe that this large diffusion rate arises from the tumour vasculature. Our results suggest that the tools developed here should be able to measure non-invasively the microvasculature in breast tumours. This would allow diagnosis of breast lesions *in vivo* and would also provide a means of following the effects of treatments, particularly treatment with anti-angiogenic pharmaceuticals.

References

1. Williams SM, Kaplan PA, Petersen JC, Lieberman RP. Mammography in women under age 30: Is there clinical benefit? *Radiology* **161**:49-51, (1986).

2. Ciatto S, Cataliotti L, Distante V. Nonpalpable lesions detected with mammography: Review of 512 consecutive cases. *Radiology* **165**:99-102 (1987).

3. Dershaw DD, Shank B, Reisinger S. Mammographic findings after breast cancer treatment with local excision and definitive irradiation. *Radiology* **164**:455-461 (1987).

4. Rosen PP, Braun DW, Kinne DG. The clinical significance of breast cancer. *Cancer* **46**:919-929 (1980).

5. Folkman J. What is the evidence that tumors are angiogenesis dependent? *JNCI* **82**:4-6 (1990).

6. Sutherland RM, McCredie JA, Inch WR. Growth of multicell spheroids in tissue culture as a model of nodular carcinomas. *JNCI* **46**:113-120 (1971).

7. Folkman J, Hochberg M. Self-regulation of growth in three dimensions. *J Exp Med* **138**:745-753 (1973).

8. Sutherland RM. Cell and environment interactions in tumour microregions: The multicell spheroid model. *Science* **240**:177-184 (1988).

9. Folkman J. Angiogenesis and breast cancer. *J Clin Oncol* **12**:441-443 (1994).

10. Guidi AJ, Fischer L, Harris JR, Schnitt SJ. Microvessel density and distribution in ductal carcinoma in situr of the breast. *JNCI* **86**:614-619 (1994).

11. Bose S, Lesseer ML, Norton L, Rosen PP. Immunophenotype of intraductal carcinoma. *Arch Pathol Lab Med* **110**:81-85 (1996).

12. Chodak GW, Haudenschild C, Gittes RF, Folkman J. Angiogenic activity as a marker of neoplastic and preneoplastic lesions of the human bladder. *Ann Surg* **192**:762-771 (1980).

13. Jensen HM, Chen I, DeVault MR, Lewis AE. Angiogenesis induced by "normal" human breast tissue: A probably marker for precancer. *Science* **218**:293-295 (1982).

14. Ziche M, Gullino PM. Angiogenesis and neoplastic progression in vitro. *JNCI* **69**:483-487 (1982).

15. Folkman J, Watson K, Ingber D, Hanahan D. Induction of angiogenesis during transition from hyperplasia to neoplasia. *Nature* **339**:58-61 (1989).

16. Lawson RN. Implications of surface temperatures in the diagnosis of breast cancer. *Can Med Ass J* **75**:309-310 (1956).

17. Sterns EE, Curtis A, Miller S. Thermography in breast diagnosis. *Cancer* **50**:323-325 (1982).

18. Amalric R, Girand D, Thommasin L. The persistently abnormal isolated infrared thermogram: The highest known risk of breast cancer. *Acta Thermographia* **3**:118-124 (1982).

19. El Yousef SJ. MRI of the breast. *Radiology* **150**:761-766 (1984).

20. Heywang SH, Wolf A, Pruss E, Hilbertz T, Eiermann W, Permanetter W. MRI of the breast with Gd-DTPA: Use and limitations. *Radiology* **171**:95-103 (1989).

21. Burns PN, Halliwell M, Wells PN, Webb AJ. Ultrasonic doppler studies of the breast. *Ultrasound in Medicine and Biology* **8**:127-143 (1982).

22. Stoica G, Koestner A, Capen C. Characterization of N-ethyl-N-nitrosourea induced mammary tumors in the rat. *Am J Pathol* **110**:161-167 (1983).

23. Maier CF, Nikolov HN, Chu KC, Chronik BA, Rutt BK. Practical design of a high-strength breast gradient coil. *MRM* **39**:392-401 (1998).

24. Chronik BA, Rutt BK. Constrained length minimum inductance gradient coil design. *MRM* **39**:270-278 (1998).

25. Rutt BK, Maier CVF. Design and construction of gradient coils for diffusion breast imaging. Invited presentation at the *Society of Magnetic Resonance Breast Imaging Workshop*, Washington D.C., June 24-25, 1995.

26. Chronik BA, Alejski A, Rutt BK. A 2000mT/m multilayer gradient coil for mouse imaging. *Proceeding of the International Society for Magnetic Resonance in Medicine* **7**:496 (1999).

27. Chronik BA, Rutt BK. Constrained Length Minimum Inductance Gradient Coil Design. *MRM* **44**:955-963 (2000).

Bibliography of Publications and Meeting Abstracts

Publications

28. Chronik BA, Rutt BK. Constrained Length Minimum Inductance Gradient Coil Design. *MRM* **44**:955-963 (2000).

29. Maier CF, Nikolov HN, Chu KC, Chronik BA, Rutt BK. Practical design of a high-strength breast gradient coil. *MRM* **39**:392-401 (1998).

30. Chronik BA, Rutt BK. Constrained length minimum inductance gradient coil design. *MRM* **39**:270-278 (1998).

Meeting Abstracts

1. Friesen-Waldner L, Gareau P, Chronik B, Rutt B. Magnetic resonance imaging techniques for the examination of tumour vasculature. *Era of Hope, Department of Defense Breast Cancer Research Program Meeting* **1**:191 (2000).

2. Chronik BA, Alejski A, Rutt BK. A 2000mT/m multilayer gradient coil for mouse imaging. *Proceeding of the International Society for Magnetic Resonance in Medicine* **7**:496 (1999).

3. Rutt BK, Maier CVF. Design and construction of gradient coils for diffusion breast imaging. Invited presentation at the *Society of Magnetic Resonance Breast Imaging Workshop*, Washington D.C., June 24-25, 1995.

Personnel Receiving Pay From this Research Effort

Individual	Position
Andrew Alejski	Research Assistant
Lanette Friesen-Waldner	Postdoctoral Fellow

Appendices

Design and Fabrication of a Three-Axis Edge ROU Head and Neck Gradient Coil

Blaine A. Chronik,[1,3] Andrew Alejski,[3] and Brian K. Rutt[1,2,3]*

The design, fabrication, and testing of a complete three-axis gradient coil capable of imaging the human neck is described. The analytic method of constrained current minimum inductance (CCMI) was used to position the uniform region of the gradient coil adjacent to and extending beyond the physical edge of the coil. The average gradient efficiency of the three balanced axes is 0.37 mT/m/A and the average inductance is 827 μH. With maximum amplifier current of 200A and receive signal sweep width of ±125 kHz, the average minimum FOV using this gradient set is 7.9 cm. The completed coil has an inner diameter of 32 cm, an outer diameter of 42 cm, and a length (including cabling connections) of 80 cm. The entire coil was built in-house. The structure is actively water cooled. Heating measurements were made to characterize the thermal response of the coil under various operating conditions and it was determined that a continuous current of 100A could be passed through all three axes simultaneously without increasing the internal coil temperature by more than 23°C. Eddy current measurements were made for all axes. With digital compensation, the gradient eddy current components could be adequately compensated. A large B_o eddy current field is produced by the Gz axis that could be corrected through the use of an auxiliary B_o compensation coil. Preliminary imaging results are shown in both phantoms and human subjects. Magn Reson Med 44: 955–963, 2000. © 2000 Wiley-Liss, Inc.

Key words: gradient coil; neck; head; minimum inductance; carotid artery; constraints; optimization; eddy current; heating; construction; MRI; edge coil; ROU; region of uniformity; coil design

There are many important imaging applications that stand to benefit from the application of higher gradient strengths and increased switching speeds produced over the human neck and head. In the neck, velocity imaging techniques are applied to examine blood flow through the carotid artery in the vicinity of the carotid bifurcation (1). It has also been demonstrated that diffusion weighted, high resolution imaging of the carotid artery atherosclerotic plaque structure is of importance in identifying plaques at risk of rupture (2). It can be shown that to achieve a b-value of 1000 sec/mm² using a square bipolar pair of gradient lobes with no inter-lobe delay in a total time of 20 msec (10 msec per lobe), a gradient strength of 145 mT/m is required (3).

This exceeds the capabilities of present-day body gradient coils by a factor of more than 3.

A brain-specific application in which gradient switching speed is important is functional MRI (fMRI). An important goal is to obtain high spatial resolution in single-shot EPI images over a brain-sized FOV (20 cm) with an echo time yielding optimal T_2^* contrast-to-noise ratio (4). For an EPI sequence without ramp sampling, a received signal sampling rate of 500 kHz and a 20-cm FOV requires a 58-mT/m gradient strength. If a 128-lobe EPI readout train is to be played out in 64 msec, trapezoidal ramp times of 150 μs or less are required.

A gradient efficiency of 0.4 mT/m/A with an inductance of less than 1000 μH was chosen as the design goal for this work, as a compromise between serving applications in need of gradient speed such as fMRI (which would argue for minimizing inductance at the expense of gradient strength), and those that demand strength such as diffusion or flow imaging (which would argue for higher gradient efficiency at the cost of increased inductance). An additional stipulation was that this strength needed to be achieved over a region of uniformity (ROU) that covered the human neck. The anatomical region of interest is centered on the carotid bifurcation, and must be large enough to image the most common sites of carotid atherosclerosis. This region spans a cylindrical volume approximately 16 cm long (inferior to superior) and 16 cm in diameter, and extends into the torso, inferior to the level of the shoulders (Fig. 1). This "edge" gradient coil can be operated in a configuration compatible with brain imaging by inserting the subject only half as far into the coil. This would provide improved visual communication with the subject during scanning, a capability of considerable importance in many fMRI studies. While commercial head-only gradient insert systems are available that meet the speed and strength specifications, they are designed for brain imaging only and are incompatible with imaging the carotid artery.

A minimum inner coil diameter of 32 cm was chosen. This is considered to be compatible with human imaging, taking into account the space required for an RF coil assembly. The total coil length was specified to be less than 80 cm, based on the need to keep the coil (which would be positioned asymmetrically within the magnet bore during operation) within a uniform region of the main magnet, thereby preventing net forces on the structure.

A recently developed gradient design algorithm was applied to obtain a three-axis gradient coil meeting the specifications described above. A prototype coil was constructed, and the thermal response was tested to determine whether heating represents a significant limitation to operation. The coil was not shielded and the eddy currents were measured in order to determine the required com-
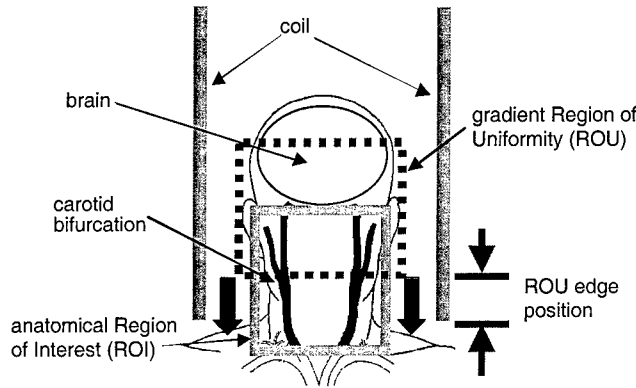
FIG. 1. Summary of the design problem. The ROU (dashed box) must be positioned to overlap the anatomic ROI (solid box) covering the carotid bifurcation. For a head-sized gradient coil, the ROU must be placed such that it extends beyond the edge of the coil.

pensation. The coil was operated in magnets of three different field strengths (0.5T, 1.5T, and 4.0T). Finally, preliminary imaging tests in both phantoms and human subjects were conducted to demonstrate the achieved gradient uniformity and image quality.

METHODS

Axis Design

All coil designs were obtained using the method of constrained current minimum inductance (CCMI) (5). The CCMI method extends analytic minimum inductance target field techniques to solve for the minimum inductance coil design subject to constraints on both the magnetic field and current density (6).

The quantities of interest in edge gradient coil design are depicted schematically in Fig. 2: They are the length of the coil, the size of the ROU, and the proximity of the ROU to the edge of the coil. Each quantity is normalized to the coil radius, a, to obtain scale independent measures. The aspect ratio (AR) is defined as the ratio of the length of the coil to the coil diameter. The relative ROU ($RROU$) is the length of the ROU divided by the coil radius. ROU length was chosen as a simple way to quantify the size of the ROU because the ROU diameter is generally larger than, and scales with, this length. The distance from the outer edge of the ROU to the outer edge of the coil, divided by the radius, is defined as δ. Negative values of δ indicate an ROU extending outside the coil. Gradient uniformity is defined in terms of the percent deviation in the magnitude of the derivative of B_z with respect to the relevant spatial direction defining that gradient axis. Unless stated otherwise, 30% deviation contours are used for quantification. The scale independent quantities (AR, $RROU$, δ) define a 3D parameter space over which coil performance is evaluated.

A figure-of-merit was used to quantify gradient performance (5,7):

$$M = \frac{\eta \cdot a^{2.5}}{\sqrt{L}} \qquad [1]$$

where η is the gradient efficiency (in mT/m/A) within the edge ROU, L is the coil inductance, and a is the coil radius. M is independent of both coil radius and the number of wires used to discretize the current density.

Of practical importance is how to parameterize the constraint space input to the CCMI algorithm. The positioning of the constraints for both transverse and longitudinal axes is shown in Fig. 3a. The aspect ratio is specified by the position of the current constraints. The field constraints are placed at a radius c and positioned with spacing d along the z direction. The combination of these two constraint parameters effectively controls the size of the resulting $RROU$. The distance from the outermost field constraint to the innermost current constraint is defined as e, which controls the resulting δ. Field constraints are only required on the plane defined by $\phi = 0$ because in the implementation of the CCMI algorithm, the azimuthal variation of the current density is assumed to be either sinusoidal (transverse axes) or constant (longitudinal axes) (5).

The values of the field constraints for transverse and longitudinal axes are shown in Fig. 3b and c, respectively. For transverse axes, the relative values of the field constraints are constant along the z direction, thereby specifying a uniform transverse ROU. For longitudinal axes, the field constraint values vary linearly along the z direction; furthermore, the value of the smallest (i.e., outermost) field constraint is introduced as a separate parameter to control the relative offset of the field constraint values from zero. This constraint parameter is indicated as B_{offset} in Fig. 3c. This parameter is used because the field is not required to pass through zero at the center of the ROU as is normally the case for all central ROU designs and transverse edge ROU designs. The natural field fall-off from the coil provides the Gz gradient, and the field constraints are placed to increase its linearity. This effect is illustrated in Fig. 4.

Fabrication

The wire used for the coil was composed of 12 strands of 1.02-mm-diameter copper wire arranged in a Litz braiding to produce a wire with a rectangular cross section of 2.5 × 7 mm^2 (New England Electric Wire Corporation). Individ-
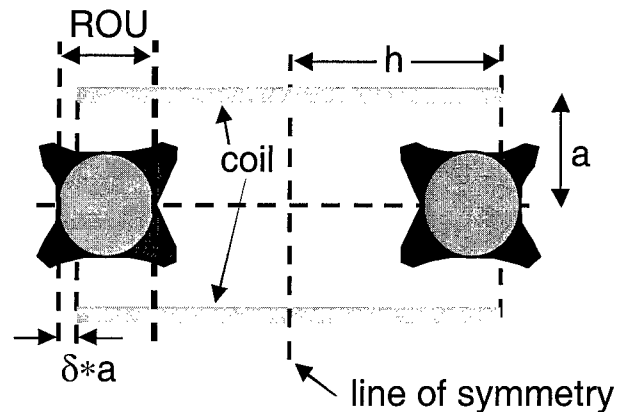

FIG. 2. Quantities of importance in edge ROU coil design are coil radius (a), length (2h), imaging region size (ROU), and imaging region position with respect to the edge of the coil (δ∗a).

ual conducting elements were coated with insulation heat
rated to 150°C. Litz wire was used in place of solid copper
to reduce resistance at frequencies of several kilohertz,
expected to be the dominant operating frequency of the
coil for high-speed imaging sequences. The DC resistance
of the wire was 2 mΩ/m. The multistrand formation of the
Litz wire also improved its workability; by comparison,
winding the transverse axis patterns with an equal area of
solid copper wire was found to be very difficult.

The winding pattern was produced using a numerically
controlled mill over the outside of the cylinders and the
wire was hand-wound into the milled grooves. A light
coating of epoxy was applied to hold the wire in place and
to fix a type-E thermocouple at the location of maximum
wire density. These thermocouples allow active tempera-
ture monitoring of the hottest areas of the coil. The pattern
for each layer was wound with one continuous length of
wire to avoid solder connections within the wall of the
coil, the most probable site for thermal failure.

Copper tubing (7 mm diameter) capable of carrying
forced-water cooling at flow rates of up to 11 l/min was
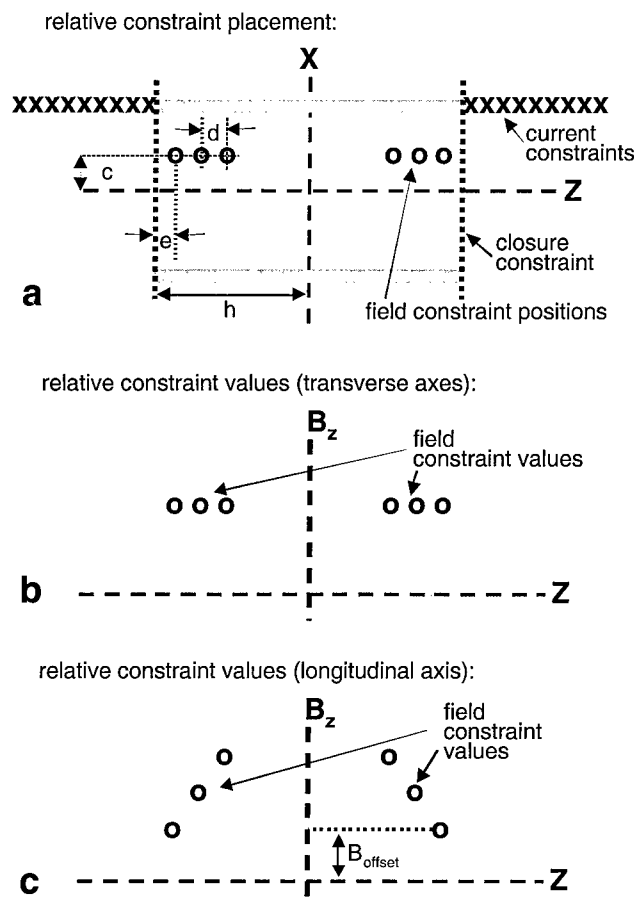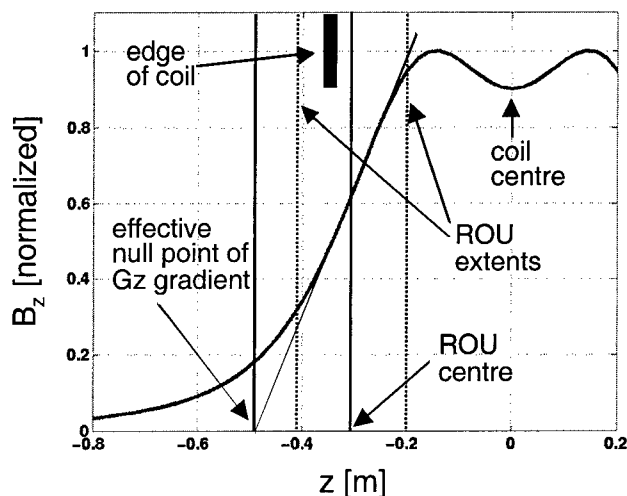plotted between the X and Y axes and the Y and Z axes of

FIG. 4. Example representation of the B_z field profile (solid curve) along the z-axis of an edge longitudinal gradient coil, indicating the offset of ROU position from the coil center. The edge of the coil is indicated by the heavy bar. The gradient efficiency is determined by the slope of the field profile at the z coordinate of the ROU center. The center of the coil is at $z = 0$. Note that the effective null point of the gradient field is at neither the center of the ROU nor the center of the coil.

FIG. 3. Parameterization of input constraint space for CCMI algo-
rithm. Constraint positions for both transverse and longitudinal axes
are shown in **a.** Field constraint values for transverse and longitu-
dinal axes are shown in **b** and **c,** respectively. Current constraint
values are always set equal to zero. B_{offset} is the value of the
smallest (i.e., outermost) field constraint.

the coil. The epoxy potting compound (Durapot 865, Co-
tronics Corporation, New York) was specially chosen to
have a high thermal conductivity (2.8 W/m/K) allowing
efficient heat transfer from the winding layers to the two
cooling layers.

Before using the coil in an MR scanner, a fixation mech-
anism was built to prevent motion of the coil within the
magnet bore during normal operation and in the event of
any failure modes the coil might experience. An external
frame was constructed to encase the coil, which was sub-
sequently attached to the external housing of the main
magnet. The frame held the coil from front to back as well
as encasing it top to bottom and side to side. The frame
was composed of 2.54-cm phenolic plates (front and back)
and 5-cm × 10-cm beams (longitudinal). The bottom
beams of the frame extended out the back of the magnet
bore along the table tray and were attached to support
beams mounted to the rear of the scanner. In Fig. 5, the
completed gradient coil is shown being installed into the
1.5T scanner.

Heating Measurements

Coil heating was tested in a series of experiments in which
$100A_{rms}$ was passed through all axes simultaneously,
while water-flow rates of 0, 6, and 11 l/min were applied.
These conditions were chosen as representing an extreme
case of gradient coil operation. Heating was halted when
internal coil temperatures increased by 50°C.

The model used to describe the temperature increase
(ΔT) as a function of time is (8,9):

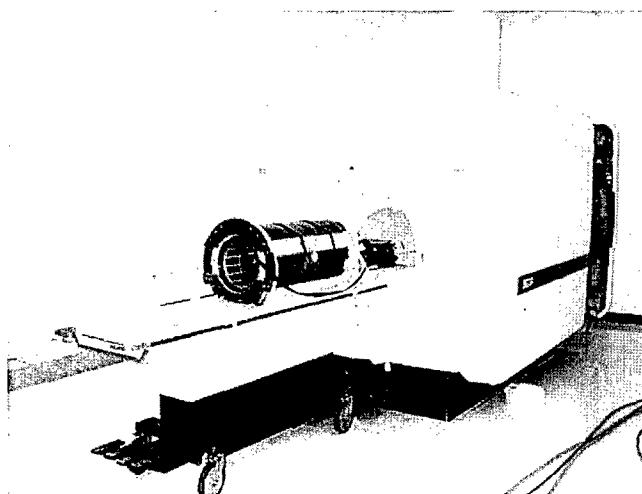$$\Delta T(t) = \Delta T_{ss} \cdot (1 - e^{-t/\tau}) \qquad [2]$$

FIG. 5. The completed neck gradient coil being installed into the 1.5T GE Signa scanner. The coil was inserted from the front of the magnet and secured at the back. The coil was transported into and out of the magnet room using the standard scanner patient bed.

where ΔT_{ss} is the steady state temperature rise and τ is a time constant describing the rate at which steady state is achieved. Equation [2] was fit to the experimental data to obtain values for ΔT_{ss} and τ for each level of water cooling.

Electrical Measurements and Gradient Efficiency

Bench top measurements of both resistance and inductance were made at frequencies of 120 Hz, 1 kHz, and 10 kHz using a Hewlett-Packard 4262A LCR meter.

The completed coil was interfaced with both a Varian-Siemens Unity INOVA 4T whole body scanner (peak current: 250A, peak voltage: 600V), a 1.5T General Electric Signa Horizon with Echospeed gradient amplifiers (peak current: 200A, peak voltage: 1200V; General Electric Medical Systems, Milwaukee, WI), and a 0.5T General Electric Signa Scanner (peak current: 84A, peak voltage: 200V). Various RF coils were constructed and tuned to resonate within the bore of the gradient coil.

The gradient efficiency for each axis was measured by imaging a grid phantom of known dimensions using a known current and an initial guess at the efficiency (i.e., the calculated values). The reconstructed image grid was used in conjunction with the known grid dimensions to adjust the gradient efficiency until the elements of the image were reconstructed to the correct dimension. The phantom was composed of a cylindrical container filled with water (19 cm diameter, 25 cm length), containing a plastic rectangular lattice with square in-plane grid elements 16×16 mm^2. The phantom was larger than the expected ROU to allow determination of gradient inhomogeneities beyond the ROU.

Eddy Current Measurements and Compensation

Eddy currents were measured on the 4T scanner. For each axis, an RF solenoid containing a small, pure water sample was placed in two different positions, and the FIDs following an RF excitation after a gradient pulse were measured.

The derivative of the phase with respect to time of each FID gave an estimate of the instantaneous frequency, and therefore the local field, experienced by that coil as a function of time following the gradient pulse. By comparing the frequencies measured by the two solenoids and knowing the separation of the samples, the gradient and B_o components of the eddy current fields were determined.

The transient fields were fitted to a multiexponential decay curve using the method of least-squares minimization. The amplitude of the gradient eddy current fields were expressed as a percentage of the applied gradient pulse. B_o eddy current fields were expressed as a frequency shift normalized to the amplitude of the applied gradient pulse (i.e., in units of Hz/mT/m).

The 4T scanner is equipped with digital eddy current compensation allowing five different amplitude and time constant components to be added to gradient waveforms in order to compensate for the gradient field components. This scanner currently lacks a B_o compensation coil and there was no ability to directly compensate for B_o field transients. The values of the fit to the transient gradient field response were entered into the digital compensation control and the eddy currents measured again. This process was repeated iteratively until an acceptable degree of compensation was achieved.

Imaging

All human imaging was conducted on the 1.5T scanner, without any eddy current compensation. Because the inductances of the neck coil axes were significantly smaller than those of the body coil for this scanner (on average, 780 μH as compared to 1200 μH), an inductor was added in series with each axis of the neck coil to prevent oscillations in the amplifier output current and minimize pre-emphasis errors.

On the 4T scanner, gradient eddy current compensation was applied as described above. No extra inductance was required because the system was capable of accommodating inductances in the range of 300 μH to 1400 μH. A more robust fixation mechanism was implemented because of the increased forces on the coil. In its first implementation this fixation was not compatible with human imaging, and therefore all preliminary images collected were of small animals and phantoms.

RESULTS

Transverse Axis Design

Figure 6 shows a plot of M as a function of AR for a fixed $RROU$ size of 1.0 and three different values of δ (-0.2, 0.0, and 0.2). For each value of δ, increasing ARs result in higher values of M. The merit improvements plateau above certain ARs, the values of which are a function of δ.

The effects of moving the ROU with respect to the edge of the coil are more effectively visualized by examining the M contour plot of Fig. 7. The contour plot is over the axes of $RROU$ and δ, for a fixed AR of 2.3. The effect of increasing $RROU$ is generally to decrease M. For any fixed $RROU$, the dependency of M on δ displays a maximum at a value of δ, which is itself a weak function of the $RROU$.
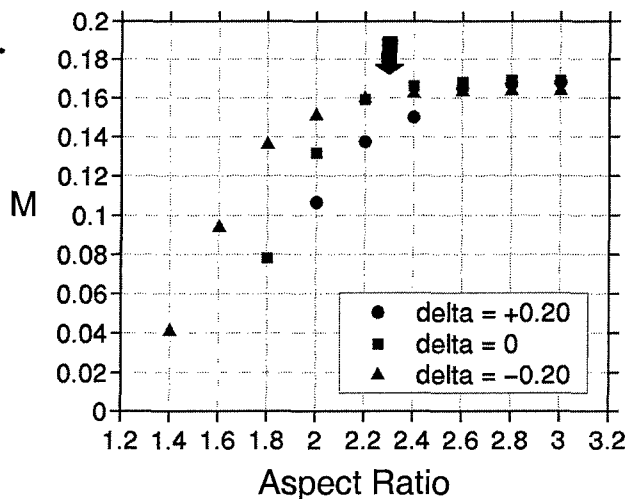
FIG. 6. Design merit (M) vs. aspect ratio (AR) for transverse coil designs of three δ values (−0.20, 0, 0.20). RROU was held constant at 1.0. The solid arrow indicates the AR taken as constant for the plot of Fig. 7.

With this design space determined, the optimal configuration for this application could be identified. Based on Fig. 6, the aspect ratio of 2.3 (indicated on the plot by the solid arrow) was chosen as the smallest value for which no decrease in *M* was associated. For an axis radius of 16.5 cm, this corresponds to a coil length of 76 cm.

With the value of *AR* chosen, Fig. 7 was consulted to fix the properties of the ROU. For a 16.5-cm radius coil the ROU specifications mentioned in the introduction corre-
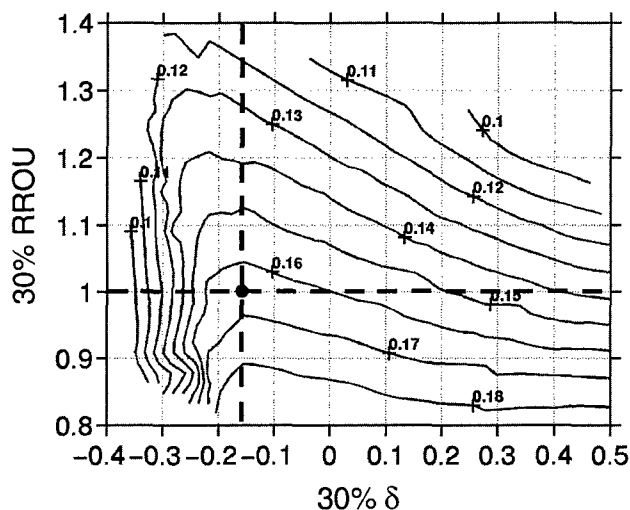

FIG. 7. A contour plot of M over the plane of constant AR = 2.3 through the transverse design parameter space. The horizontal axis indicates the position of the outer edge of the imaging region with respect to the edge of the coil as a fraction of the coil radius. The vertical axis indicates the length of the imaging region as a fraction of the coil radius. For a coil radius of 16.5 cm, the plot area above the horizontal dashed line is compatible with neck imaging. The highest performance design in the space above the ROU limit is indicated by the dot at the intersection of the vertical and horizontal dashed lines.
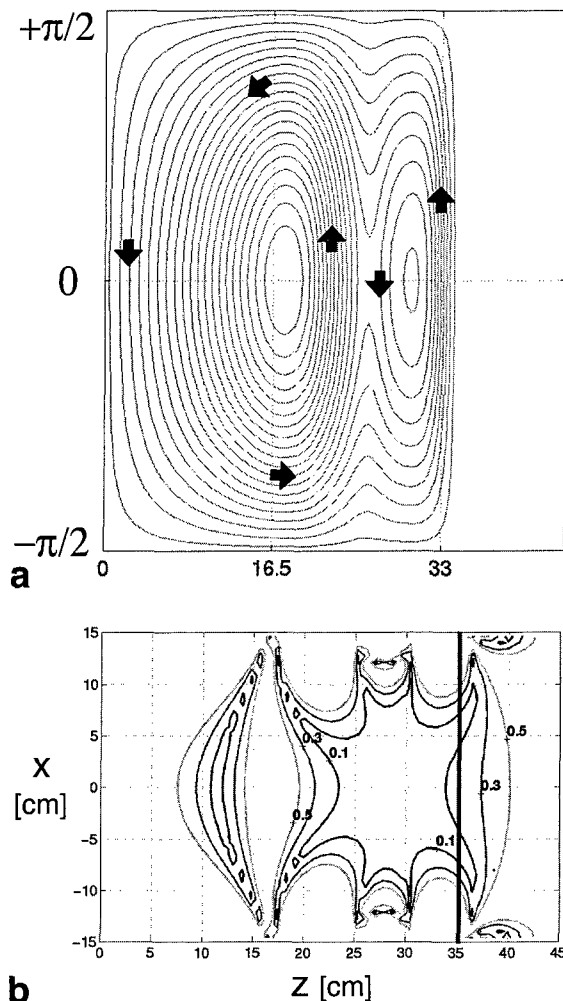
FIG. 8. Chosen transverse axis (Gx) design. **a:** Single quadrant wire pattern. Solid arrows indicate the relative current directions through the wire pattern. **b:** Calculated map of gradient uniformity over the transverse plane. The z-axes for both plots are to the same scale, and therefore the position of the ROU with respect to the wire pattern can be seen by comparing **a** and **b.** The solid bar in **b** indicates the edge of the physical coil. The Gy axis uses this same design.

spond to an *RROU* of approximately 1.0; therefore, the allowed designs occupy the region above the horizontal dashed line defining *RROU* = 1.0. The highest performance design in the remaining region of the plot corresponds to a δ of −0.16 (indicated by the vertical line of Fig. 7). This value corresponds to an ROU projecting 2.6 cm beyond the inferior end of the coil. This meets the neck imaging criterion, and therefore the coil corresponding to the design space parameter coordinate (*AR*, *RROU*, δ) = (2.3, 1.0, −0.16) was chosen as the best transverse coil design for this application.

A single quadrant of the wire pattern corresponding to this design is shown in Fig. 8a. The calculated ROU extents for 10%, 30%, and 50% deviations from uniformity are shown in Fig. 8b. The calculated performance parameters for this design (for both the x and y axes) are summarized in Table 1.

Table 1
Calculated and Measured Coil Characteristics

		X	Y	Z
Radius [m]		0.1625	0.1825	0.2025
η [mT/m/A]	Calculated	0.42	0.35	0.37
	Measured	0.40	0.35	0.35
L [μH]	Calculated [DC]	760	800	805
	120 Hz	780	820	880
	1 kHz	780	820	870
	10 kHz	770	810	860
R [mΩ]	Calculated [DC]	220	235	153
	120 Hz	227	230	160
	1 kHz	270	290	210
	10 kHz	–	–	–

Longitudinal Axis Design

Because imaging regions for all axes of a three-axis coil system must overlap for them to be useful as a group, decisions made regarding one axis have ramifications on the design of the others. Longitudinal designs display better performance than transverse designs; therefore, most effort was expended choosing the optimal transverse axis design. The longitudinal design was then simply required to be compatible with the AR and ROU placement.

The chosen design for the longitudinal axis is shown in Fig. 9. One quadrant of the wire pattern is shown in Fig. 9a. The calculated ROUs for 10%, 30%, and 50% deviations from uniformity are shown in Fig. 9b. The 30% ROU is approximately 17.5 cm long and its outer extent is 5 cm exterior to the coil. Although both of these quantities exceed the minimal specifications of matching the transverse design ROU position and size, it was determined that over the longitudinal design space this configuration represented the highest merit. The relevant performance parameters for this design are summarized in Table 1.

Heating Measurements

The measured values for ΔT_{ss} and τ are shown in Table 2. Even without cooling, the coil could be run for over 15 min before temperatures increased by 50°C. With cooling, the coil could be operated indefinitely at $100A_{rms}$ with a temperature rise of less than 23°C.

Electrical Measurements

The measured values for resistance and inductance for the three axes are summarized in Table 1. The calculated values are included for comparison. The relatively slow increase of resistance with frequency is expected because of the Litz wire construction. The calculated resistance values are generally lower than the experimental results because they assume zero frequency and do not take into account lengths of connecting wire within the coil or the effects of imperfect electrical connections.

Eddy Current Measurements and Compensation

Table 3 summarizes the results of eddy current measurements for each gradient axis, before and after compensation. Cross-axis eddy current effects were also measured for all combinations of axes, and in every case were found,
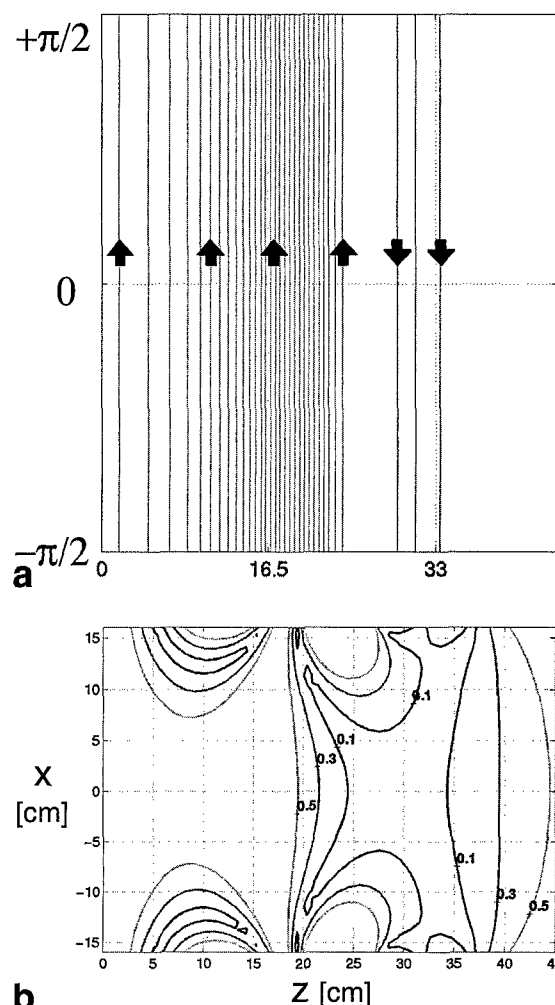
FIG. 9. Chosen longitudinal axis (Gz) design. **a:** Single quadrant wire pattern. **b:** Calculated map of gradient uniformity over the transverse plane. The z-axes for both plots are to the same scale, and therefore the position of the ROU with respect to the wire pattern can be seen by comparing **a** and **b**. The solid bar in **b** indicates the edge of the physical coil (determined by the extent of the transverse axes).

without compensation, to be smaller than 0.03% of the applied gradient. Because of the small amplitude, no cross-axis compensation was applied.

The eddy current results for the Gx and Gy axes are similar. Prior to compensation, both transverse axes were characterized by small residual gradient fields (less than 0.07%) with time constants of less than 100 msec. Compensation reduced these effects to less than 0.02%. The Gy axis displayed a small, negative B_o eddy current response, whereas the Gx axis B_o response was almost negligible.

Table 2
Heating Measurement Summary

Flow [l/min]	ΔT_{ss} [°C]	τ [s]
0	63.1	573
6	34.3	365
11	22.7	209

Table 3
Compensated and Uncompensated Eddy Current Measurements

Axis		Before compensation	After compensation
X	G_x	0.037% 63 ms	0.01%
	B_o	−0.07 Hz/mT/m 500 ms	–
Y	G_y	0.066% 34.4 ms	0.02%
	B_o	−0.55 Hz/mT/m 116 ms	–
Z	G_z	0.30% 60 ms; 0.14% 980 ms	0.1%
	B_o	21.3 Hz/mT/m 100 ms; 22.4 Hz/mT/m 517 ms	–

For the Gz axis, the gradient eddy current component was bi-exponential with a maximum residual gradient of 0.44%. With compensation this was reduced to less than 0.1%. The B_o eddy current component for the Gz axis was observed to be much larger than either of the transverse axes and was also bi-exponential. Immediately following an 80 mT/m gradient pulse on the Gz axis, the eddy current induced field offset would be approximately 3500 Hz.

The proposed mechanism for this B_o eddy current effect is shown schematically in Fig. 10. Eddy current fields produced over the image region have a different spatial dependency than the primary imaging gradient field. The gradient component of the eddy current field does not have an effective null point (i.e., extrapolated zero cross-
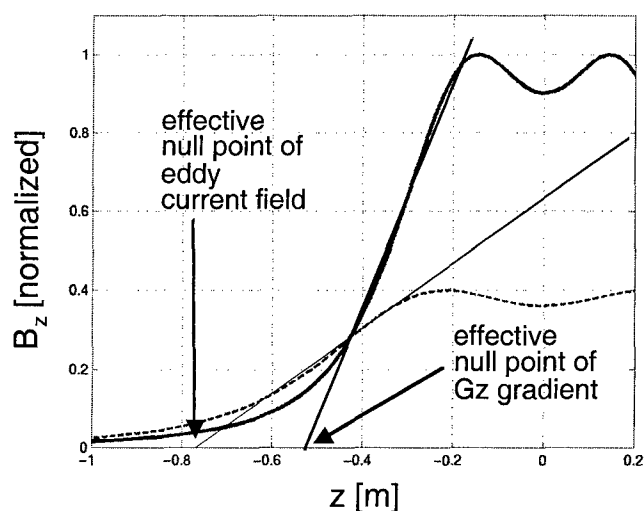

FIG. 11. Coronal (**a**) and axial (**b**) images of a cylindrical grid phantom collected using a standard body gradient coil (left) and neck gradient coil (right). Deviations from gradient uniformity result in image distortions in both cases. Individual grid elements are 16 mm square. The box indicated on the coronal images corresponds to an ROI of 16 cm square. The curved line in **b** indicates the relative position of the edge of the gradient coil.

ing) at the same location as the imaging gradient. There is therefore no current that can be applied to the gradient coil that will fully compensate for this transient eddy current. The best option would be to remove the linear variation while creating a significant field offset proportional to the difference in the positions of effective null points of the primary and eddy current-induced fields.

Imaging

Figure 11 compares images of the grid phantom collected with the neck gradient set to those collected using the whole body gradient set of the 1.5T scanner. Images were collected using a spin-echo sequence with the following parameters: TE/TR = 30/1000 msec, matrix size = 512 × 512, FOV = 36 × 36 cm² (24 × 24 cm² for axials), slice thickness = 5 mm, and number of averages = 1. The box overlaid on the coronal images indicates a region 16 cm square, corresponding to the size of the ROU over which less than 30% deviation was predicted. The most distorted grid element (in the upper corners of the box) in this region for the neck coil image was lengthened by 28% compared to the grid elements at the center of the image. The measured efficiencies at the center of the ROU for the Gx, Gy, and Gz axes were found to be 0.40 mT/m/A, 0.35 mT/m/A, and 0.35 mT/m/A, respectively. The coronal grid image obtained using the neck coil also has the edge of the coil

FIG. 10. Schematic comparison of Gz gradient field profile (solid curve) and corresponding eddy current-induced field profile (dashed curve). The effective null points of each profile are, in general, different. No amount of current can be passed through the gradient coil to compensate for the eddy current field shown above. If compensation is applied such that the gradient coil field compensates for the slope of the eddy current field, a large B_o offset would result.
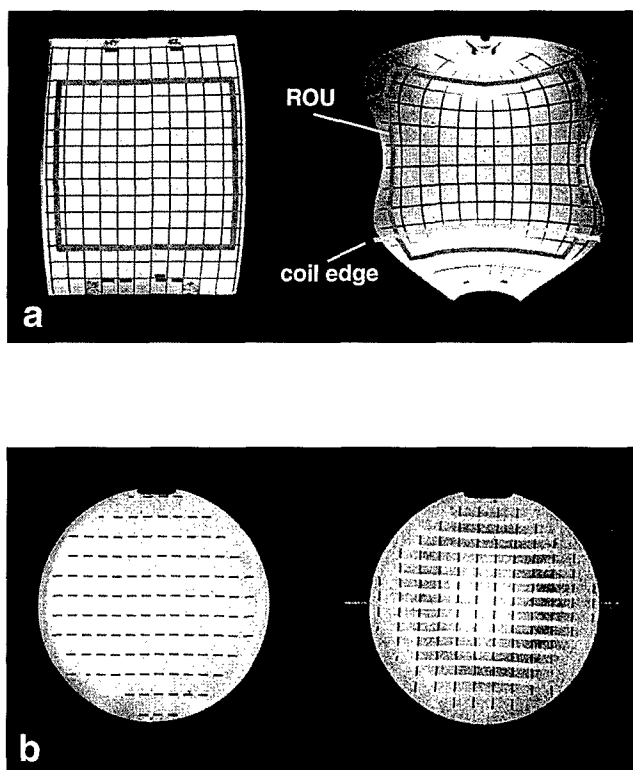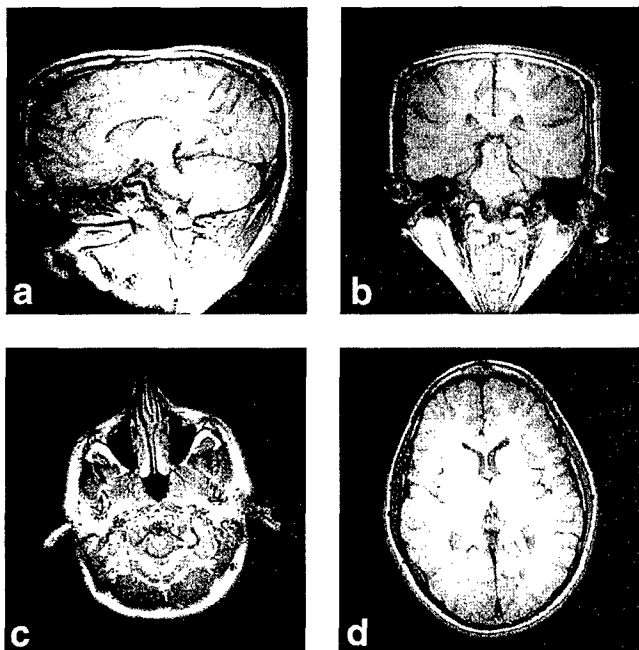
FIG. 12. Spin-echo images of the neck of a human volunteer collected at 1.5T using the neck gradient coil set. Sequence parameters common to all images were: TE/TR = 30/500 msec, number of averages = 2, matrix = 256 × 256, slice thickness = 5 mm. The sagittal and coronal slices were collected with a 36-cm FOV, whereas the axial slices were collected using a 24-cm FOV. The subject was positioned such that his eyes were even with the edge of the coil. Image c corresponds to subject anatomy 2 cm beyond the physical edge of the coil. Image d corresponds to a position approximately 5 cm within the coil. A shielded birdcage RF coil was used in all cases.

indicated. The region of expected 30% deviation extends 2.5 cm beyond the edge of the coil, as predicted.

Figure 12 shows images of human subjects collected at 1.5T. Images were collected using a spin-echo sequence with the imaging parameters indicated in the figure captions. The subject was positioned with eyes at the physical edge of the coil such that the brain was within the ROU. Image distortions at the periphery of the head are clearly visible in both the sagittal and coronal images. The severe distortion in the neck region is expected, as the gradient strength drops quickly with the distance outside the coil. A shielded volume birdcage RF coil specifically tuned to operate within the gradient coil was used. The use of a copper mesh shielding for the RF coil created severe eddy currents, and as a result the maximum gradient strengths had to be limited to 44 mT/m for these scans.

Figure 13 shows a series of coronal and axial spin-echo images of the human neck collected in the same scanner. In these images the subject was positioned all the way into the coil until the shoulders came into contact with the coil edge. Two 3-inch RF surface coils were placed on either side of the neck and operated as a phased-array. The pulse sequence was not optimized for use in the neck, where motion is the cause of the ghosting artifacts visible on the coronal images.

DISCUSSION

The power of the CCMI method was fully exploited in the design of a very high strength three-axis gradient coil capable of imaging the human neck in the vicinity of the carotid arteries. The design was chosen as a compromise between speed and strength, intended to offer significant improvements in both fast-pulse sequences (such as EPI and FSE) as well as high-resolution diffusion and velocity-encoding sequences.

There are three good designs in the literature (reports in which gradient coils were designed, built, and tested on human subjects) against which this gradient coil can be directly compared, and they are summarized in Table 4. The innermost axis of each design has been listed in each case. The efficiency values have been scaled to correspond to a fixed inductance of 780 μH for each design; however, the fact that the radii and ROU sizes of the respective designs are different should still be kept in mind when comparing the efficiency values. It is clear from Table 4 that the design presented here has advantages in imaging in the vicinity of the edge of the coil. This design is intrinsically more efficient than all but the Alsop design; furthermore, the edge design is the only one capable of
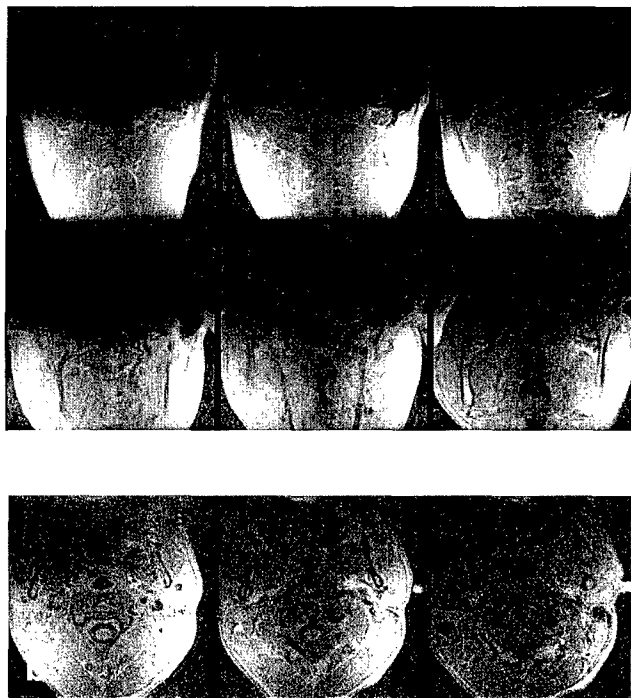
FIG. 13. Spin-echo images of a human volunteer collected at 1.5T using the neck gradient coil set. Sequence parameters common to all images were: TE/TR = 9/800 msec, number of averages = 1, FOV = 16 × 16 cm, matrix = 256 × 192, slice thickness = 5 mm, slice spacing = 5 mm. The subject was positioned such that his shoulders were in contact with the edge of the coil. The axial slices in b were obtained with the left image collected approximately 6 cm in from the edge of the coil and the subsequent images moving further in. This is the vicinity of the carotid bifurcation. Two 3-inch surface RF coils were used in phased-array mode in all images. The signal falloff with slice position evident in b is due to the sensitivity falloff away from the surface RF coils.

Table 4
Selected Head Gradient Coil Designs From the Literature

Design	Radius (inner)	ROU (5%)	δ (5%)	L [μH]	η [mT/m/A]
Abduljalil et al. (1994)	13.6 cm	~15 cm	~9 cm	780	0.35
Alsop et al. (1996)	16 cm	~16 cm	~9 cm	780	0.59
Bowtell et al. (1999)	19 cm	~18 cm	~10 cm	780	0.13
Edge design (Gx)	16 cm	~12 cm	~0 cm	780	0.40

imaging inferior to the carotid bifurcation in human subjects.

The attainment of edge gradient coil designs represents a significant advance; however, the construction and characterization of a workable three-axis coil set that is truly compatible with human scanning is equally important. The completed coil is capable of handling the continuous application of the full output of most clinical amplifiers with only modest water cooling. This ability is very important because it allows sequences to truly utilize the strength and speed improvements offered by this design.

The results of eddy current measurements conducted with this unshielded coil were for the most part encouraging. For the transverse axes, the induced eddy current gradient fields were measured to be very small prior to compensation, and negligible (for routine imaging applications) afterwards. The response of the z axis was dominated by a large transient B_0 field component. It is possible to implement a B_0 compensation coil on the 4T scanner and this is a likely direction for future work with this system.

The performance improvements available with this coil set were demonstrated in imaging experiments that progressed from phantoms to humans. The predicted uniformity was achieved over a region extending outside of the coil, and this was used to advantage in the collection of the human neck images. It was also demonstrated that the coil could provide usable images of the brain for subjects positioned with eyes just outside the physical edge of the coil. This should represent an interesting advantage for the fMRI applications referred to in the introduction. The issue of magnetostimulation thresholds in humans when using this coil has been investigated by the authors and will be reported in a separate publication.

REFERENCES

1. Steinman DA, Rutt BK. On the nature and reduction of plaque-mimicking flow artifacts in black blood MRI of the carotid bifurcation. Magn Reson Med 1998;39(4):635–641.
2. Shinnar M, Fallon JT, Wehrli S, Levin M, Dalmacy D, Fayed ZA, Badimon JJ, Harrington M, Harrington E, Fuster V. The diagnostic accuracy of ex vivo MRI for human atherosclerotic plaque characterization. Arteriosclerosis, Thrombosis, and Vascular Biology 1999; 19(11):2756–2761.
3. Callaghan PT. Principles of nuclear magnetic resonance microscopy. New York: Oxford University Press, 1991.
4. Gati JS, Menon RS, Ugurbil K, Rutt BK. Experimental determination of the BOLD field strength dependence in vessels and tissue. Magn Reson Med 1997;38:296–302.
5. Chronik BA, Rutt BK. Constrained length minimum inductance gradient coil design. Magn Reson Med 1998;39:270–278.
6. Turner R. Minimum inductance coils. J Phys E 1988;21:948–952.
7. Turner R. Gradient coil design: a review of methods. Magn Reson Imag 1993;11:903–920.
8. Chu KC, Rutt BK. MR gradient coil heat dissipation. Magn Reson Med 1995;34:125–132.
9. Chronik BA, Alejski A, Rutt BK. Design and fabrication of a three-axis multilayer gradient coil for magnetic resonance microscopy of mice. MAGMA 2000;10:131–146.
10. Alsop DC, Connick TJ. Optimization of torque-balanced asymmetric head gradient coils. Magn Reson Med 1996;35:875–886.
11. Abduljalil AM, Aletras AH, Robitaille P-ML. Torque free asymmetric gradient coils for echo planar imaging. Magn Reson Med 1994;31:450–453.
12. Bowtell R, Peters A. Analytic approach to the design of transverse gradient coils with co-axial return paths. Magn Reson Med 1999;41:600–608.

Appendix II

The pulse sequence and the analysis program developed for this grant were tested with two substances – water and acetone - whose diffusion coefficients are well documented. The theoretical and experimentally determined results are shown below for diffusion encoding along six unique directions:

Water:

The theoretical value of the diffusion coefficient of water is between 2.12×10^{-3} and 2.63×10^{-3} mm^2/s at 21.7 C°.

Diffusion Encoding Direction	Diffusion Coefficient (mm^2/s)
xy	$2.03 \pm 0.02 \times 10^{-3}$
-xy	$2.10 \pm 0.09 \times 10^{-3}$
xz	$2.08 \pm 0.10 \times 10^{-3}$
-xz	$1.97 \pm 0.06 \times 10^{-3}$
yz	$2.07 \pm 0.04 \times 10^{-3}$
-yz	$2.07 \pm 0.11 \times 10^{-3}$

Acetone:

The theoretical value of the diffusion coefficient of acetone is between 3.88×10^{-3} and 4.43×10^{-3} mm^2/s at 21.7 C°.

Diffusion Encoding Direction	Diffusion Coefficient (mm^2/s)
xy	$4.47 \pm 0.04 \times 10^{-3}$
-xy	$4.59 \pm 0.05 \times 10^{-3}$
xz	$4.62 \pm 0.03 \times 10^{-3}$
-xz	$4.30 \pm 0.05 \times 10^{-3}$
yz	$4.47 \pm 0.06 \times 10^{-3}$
-yz	$4.55 \pm 0.06 \times 10^{-3}$

Reference: Bammer R, *et al.* Diffusion-weighted imaging with navigated interleaved echo-planar imaging and a conventional gradient system. *Radiology* **211**:799 (1999).

Appendix III

Figure 1
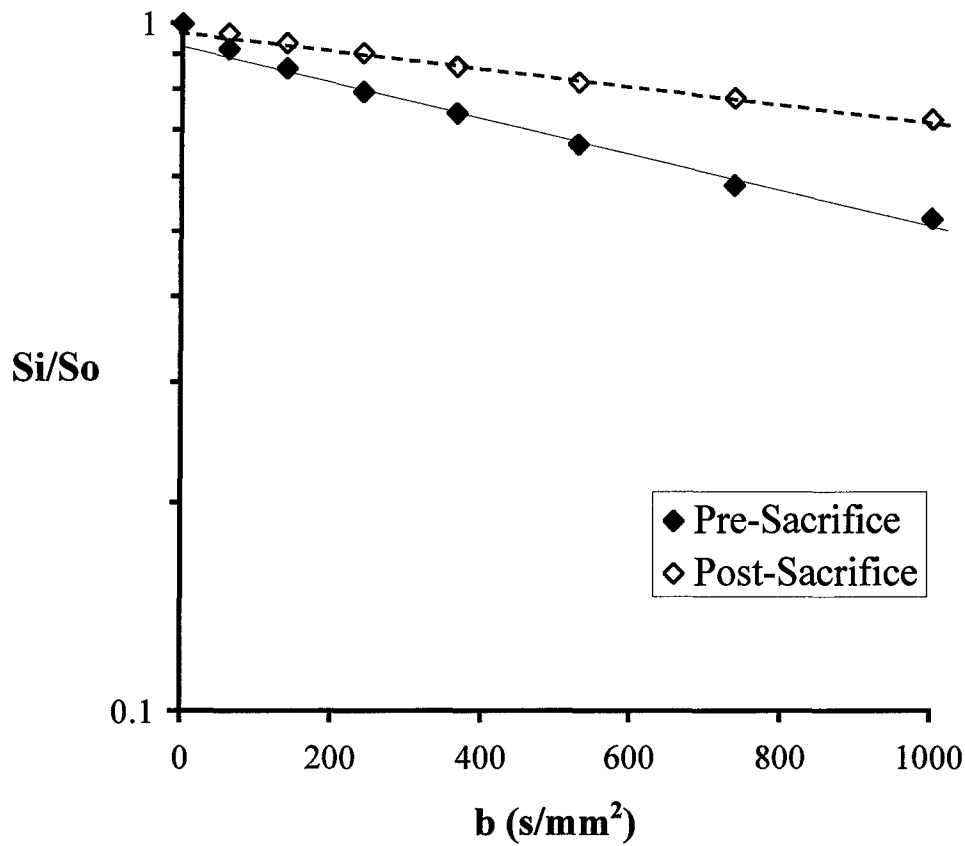
Diffusion decay curves obtained from one tumour pre-sacrifice (closed symbols) and post-sacrifice (open symbols). The straight lines show the deviation of the curves from mono-exponential behaviour for the pre-sacrifice (solid line) and post-sacrifice (dashed line) cases. Note that for both cases, the decay curves are at least bi-exponential and that the post-sacrifice curve does not decay as quickly at the outset as the pre-sacrifice curve.

Appendix III

Figure 2
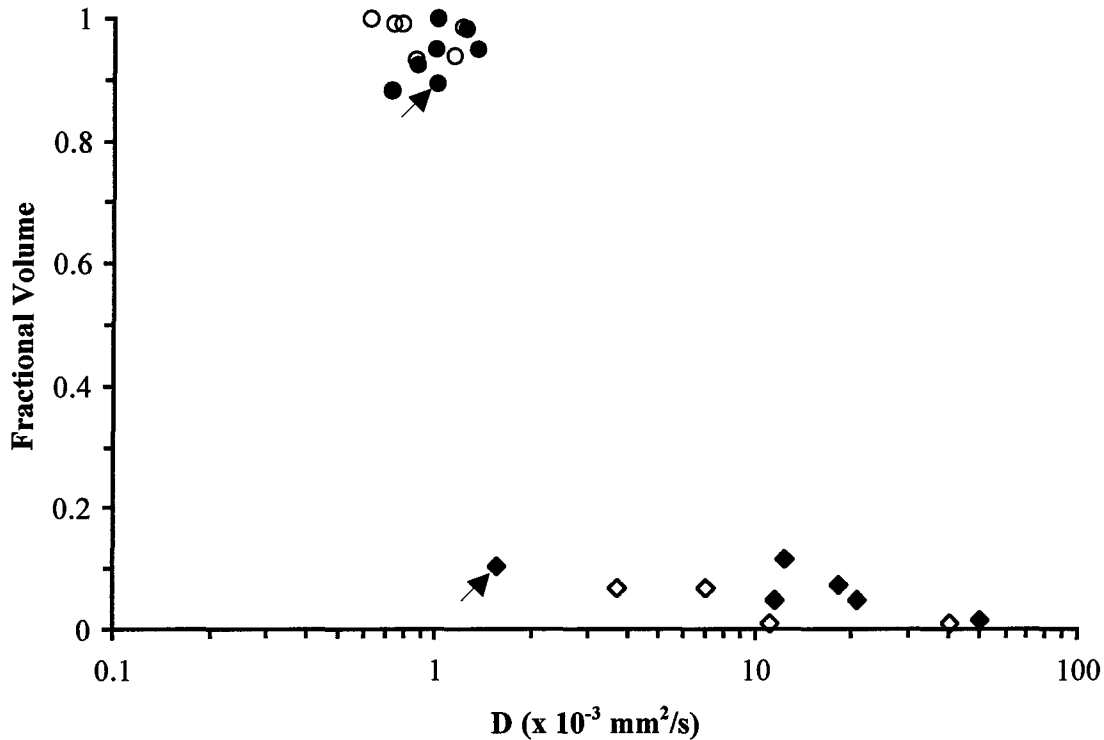
Plot of the diffusion coefficients obtained from decay curves with a maximum b-value of 1000 s/mm^2. Diffusion coefficients were derived from decay curves acquired from seven tumours pre-sacrifice (closed symbols) and post-sacrifice (open symbols). In five of the seven cases, both a low diffusion coefficient (circles) and a high diffusion coefficient (diamonds) were found for the pre-sacrifice curves. In one case, only a low diffusion coefficient was found, and in another case, two coefficients were found but they were not well differentiated (low and high coefficients are marked above by arrows). Post-sacrifice, two diffusion coefficients were still found in four of the decay curves, but the higher coefficient was now intermediate between the pre-sacrifice, high and low coefficients. These results suggested that a third diffusion rate is present.

Appendix III

Figure 3

Plot of the diffusion coefficients obtained from decay curves with a maximum b-value of 5000 s/mm^2. Diffusion coefficients were derived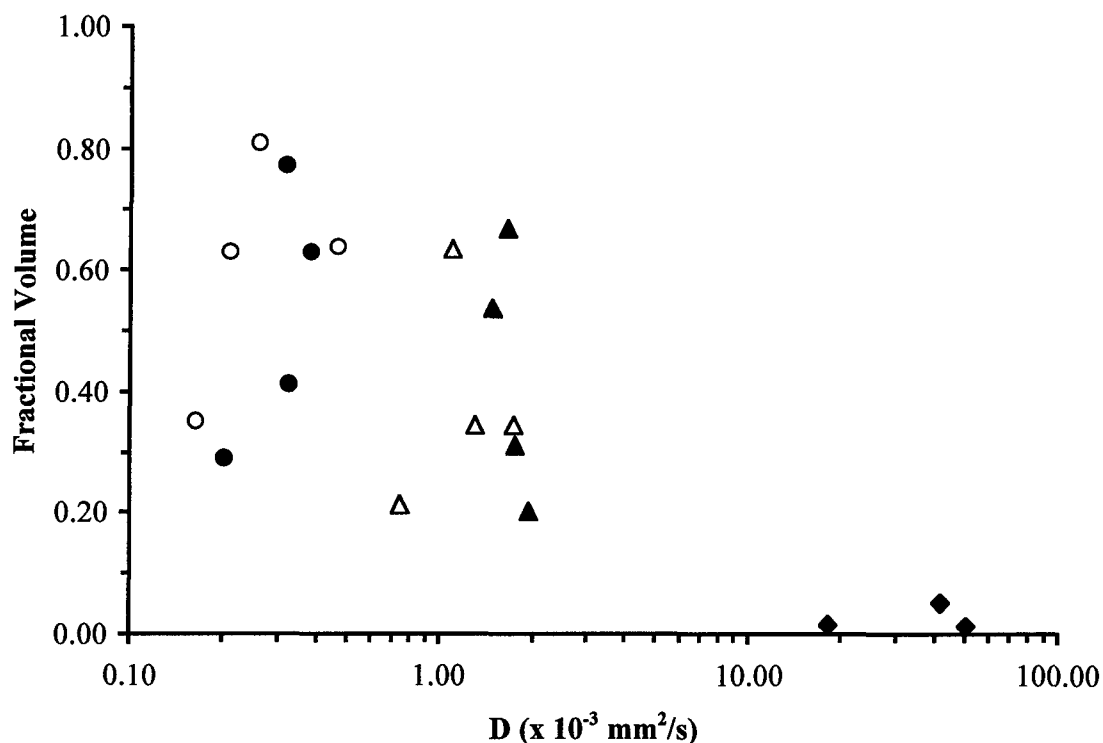 from decay curves acquired from four tumours pre-sacrifice (closed symbols) and post-sacrifice (open symbols). In three of the four cases, three diffusion coefficients were found for the pre-sacrifice curves - low (circles), intermediate (triangles) and high diffusion coefficients (diamonds). In one case, only low and intermediate diffusion coefficients were found. Post-sacrifice, low and intermediate diffusion coefficients were still seen, but the higher coefficient was absent in each case.

Practical Design of a High-Strength Breast Gradient Coil

Cynthia F. Maier, Hristo N. Nikolov, Kenneth C. Chu, Blaine A. Chronik, Brian K. Rutt

A high-strength three-axis local gradient coil set was constructed for MRI of the breast. Gradient fields with good uniformity (<10% deviation from the desired gradient) over most of the volume required for breast imaging were generated with efficiencies of up to 3.3 mT/m/A. The coils will allow diffusion breast imaging in clinically acceptable examination times. The electrical design, water cooling system, and fabrication techniques are described. Preliminary tests of the coil included images of a grid phantom and diffusion measurements in a short-T_2 agarose gel phantom.

Key words: breast imaging; diffusion imaging; gradient coils.

INTRODUCTION

In this paper, we present a specialized gradient coil design for breast imaging and demonstrate the utility of this coil for performing MR diffusion imaging with short-duration, high-strength gradient pulses. Sensitization of an MR pulse sequence to motion can be achieved using conventionally available gradient hardware; however, measurement of water diffusion (or slow flow in microvessels) with this hardware requires long echo times to achieve large gradient moments and therefore suffers from significant signal loss due to T_2 relaxation and system nonidealities. In addition, increasing the time between motion-sensitizing gradient pulses allows more macroscopic motion to occur in this interval, resulting in pixel misregistration, motion-induced ghost artifacts, and diffusion/flow measurement artifacts. Higher-strength gradients will allow adequate sensitization to small motions (i.e., large gradient moments) with very short, high-amplitude gradient pulses and minimal time delay between these pulses.

METHODS

The gradient coil assembly was designed in a cylindrical geometry, with each gradient coil built onto a separate cylindrical former. The three-axis coil set was composed of concentrically nested coils, oriented vertically such that their common axis was transverse to the main field as shown in Fig. 1. Space restrictions within the magnet bore require that the coils be as short as possible in the vertical direction to allow a patient to lie comfortably above the top edge of the cylinders. Unfortunately, decreasing the height of the coils (relative to their diame-

ters) makes the creation of uniform gradients within the coils much more difficult. To satisfy the competing demands of good gradient uniformity and height restrictions, we used an aspect ratio of approximately 1:1 for our cylindrical coils. The height of the complete coil assembly was 16 cm, leaving 34-cm clearance in the vertical direction in our General Electric (GE) Signa Horizon scanner (General Electric Medical Systems, Milwaukee, WI), and the largest coil diameter was 21.6 cm.

To generate the winding densities required for high gradient strengths, relatively small-diameter wire (AWG no. 20) was used to construct the coils. The resistivity of this wire is high, requiring an active cooling system to remove heat and maintain temperatures inside the coils within a range comfortable for the patient. Water-cooling jackets with very thin walls were sandwiched between the gradient coils, so that resistive heat could be removed efficiently while maintaining the compact construction of the coil assembly. A dedicated RF coil and shield were mounted inside the innermost gradient coil with an approximately 1.3-cm space between the RF coil and closest gradient coil. The entire assembly is depicted in cross-section in Fig. 2.

Electrical Design

The highly efficient quadrupolar current distribution (1–3) was used to provide gradients in B_z along both the x and z directions (G_x and G_z). This current density varies azimuthally as $\cos(2\theta)$ and is entirely directed along the axial direction on the surface of the cylindrical former. Discrete wire positions approximating the continuous quadrupolar current density were calculated by sampling the current density $\cos(2\theta)$ at θ_i such that $\cos(2\theta_{i+1}) - \cos(2\theta_i)$ was constant. A schematic diagram showing this ideal wire distribution is given in Fig. 3a. The current pattern in Fig. 3a is nonphysical in that the current is discontinuous at the ends of the coil, and therefore, connecting paths between the wires ("return wires") must be provided. In most imaging applications in which local gradient coils have been used previously, the volume to be imaged has been located at the center of the coil, and placing return paths near the ends of the cylinder had a minimal effect on the desired field within the object. For breast imaging applications, the required location for the region of good gradient uniformity is near the top edge of the coils and a conventional return wire arrangement would corrupt the gradient field uniformity within this volume. We chose to place the return wire components instead on horizontal plates at the tops and bottoms of the coils. Close to the cylinders on the plates, the return paths were extended along the z direction for at least 5 cm (no B_z is generated by current in the z direction). The bottom set of return wires for the G_z coil were strung across the bottom of the cylinder in the z direction. The quadrupole current distribution for G_x is rotated 45° with respect to G_z, and the return wires for G_x could not be strung in the z direction; therefore, these wires were located on a horizontal plate.
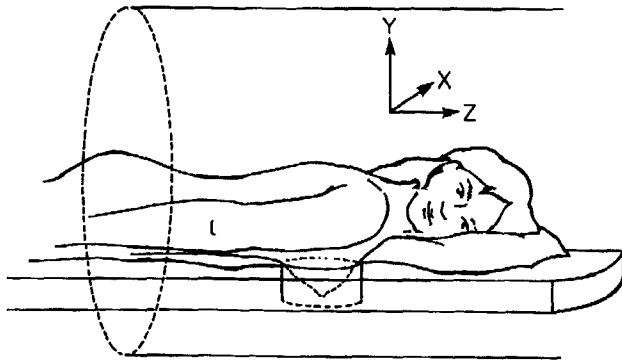
FIG. 1. Schematic showing orientation of local breast gradient coil in magnet.

The design of the G_y gradient makes use of the fact that $\nabla \times B = 0$ throughout any region in which the current density is 0. This means that a transverse gradient coil with its axis along z (the conventional orientation) can be turned 90° about the x axis so that its axis is along the y direction and used to produce a gradient in B_z along the y direction. We designed a transverse gradient coil in the conventional orientation using the target field method (4, 5) and then rotated the coil to produce G_y. Although a wide range of breast sizes exist, we defined an average volume of interest (VOI) for breast imaging (by comparison with commercially available breast RF coils) as a cylindrical volume with length equal to 60% of the coil height (11.5 cm), a diameter equal to 90% of the RF coil diameter (13.5 cm), and location flush with the top surface of the gradient coil assembly. The target field coil was designed to have its region of good gradient uniformity centered on this VOI. This design consisted of only two sets of closed current loops (Fig. 3b). For the target-field coil in its conventional orientation with its axis along z, the desired gradient is created almost entirely by the current in half of the wire loops only (the "primary" component of the loop as indicated in Fig. 3b), and return wires are an intrinsic part of the design (labeled "return" in Fig. 3b). For this coil, only one set of "return paths" is required for current continuity, and in the vertical orien-
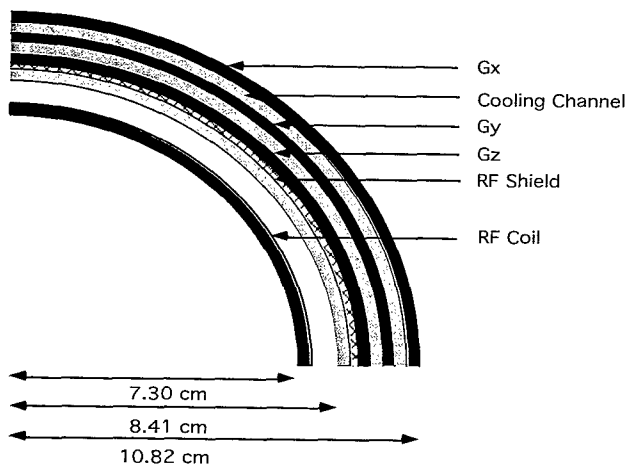
FIG. 2. Cross-section of complete gradient coil assembly showing location of RF coil and water-cooling modules.
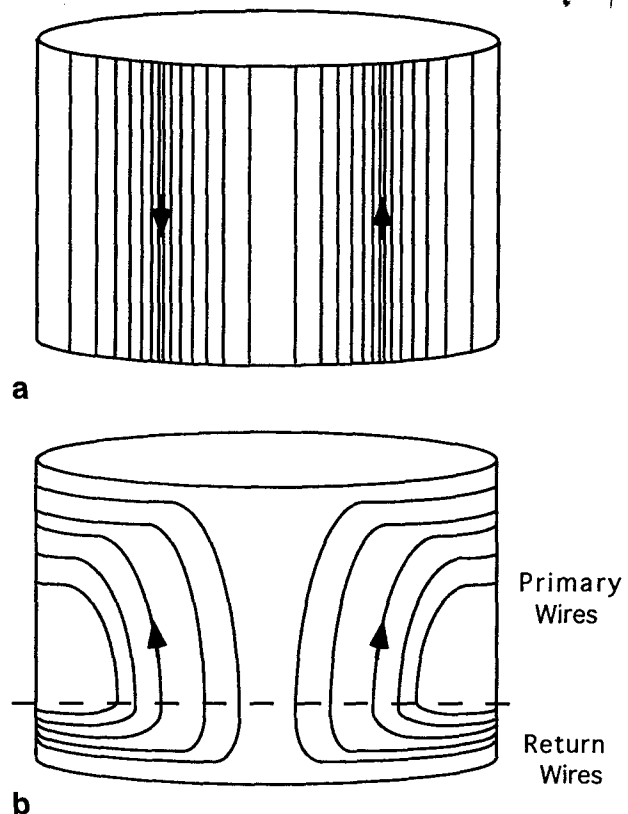
FIG. 3. (a) Quadrupolar current density with 56 windings. (b) Target-field-design transverse coil. The "primary wire" component is almost entirely responsible for generation of the transverse gradient for the conventional coil orientation with its axis along z.

tation, these wires are located at the bottom of the cylinder. In our coil design, such a large number of loops was required to generate the desired gradient efficiency that these return wires would have occupied a large fraction of the space available on the surface of the cylinder. Due to the strict limitations on coil height, we believed that this space could be used more efficiently if only the primary component of the coil design was present on the cylinder itself and the return paths were located on a horizontal plate as for the quadrupole coils. A complication that arises from truncating the wire pattern in the vertical dimension in this way is that the reciprocity relations from Maxwell's equations no longer hold for a nonphysical current distribution (i.e., $\nabla \times B \neq 0$ for a current distribution with nonzero divergence). This means that the gradient field calculated for the truncated design is not identical in the conventional and transverse orientations unless the return wires are included in the calculation. We shall see in the Results section that the truncated coil in the transverse orientation has both an increased gradient efficiency compared to the full design for the same coil height and, additionally, the region of acceptable gradient uniformity (<20% deviation from uniformity) is significantly larger for the truncated coil.

One undesirable side effect that arises from locating the return wires on horizontal surfaces is that the torque on the coils from interaction with the main static field is greatly increased. This effect is significant. For our 1.5-T

magnet, current is only supplied when the coils are positioned near the central, highly homogeneous region of the magnet (typical clinical imaging systems have a 50-cm-diameter spherical volume of better than 10 ppm B_0 uniformity) and the upward (downward) force on the $+z$ ($-z$) half of the horizontal plate for the G_z coil is approximately 15 N/A (3.5 lb/A) increasing linearly with applied current. As the gradients are switched, the effect of this force is to create an alternating torque of approximately 3 Nm/A in size. For many pulse sequences, the direction of the current is switched rapidly, resulting in a torque that alternates direction rapidly and causes significant vibrational stress on the coils. For our preliminary experiments, a temporary coil support was constructed from wood- and glass-reinforced phenolic. The horizontal plates were rigidly attached to the support, and the support structure itself served to mount the coil assembly inside the bore of the imager, thereby preventing any bulk coil motions that could arise from the magnetic forces on the wires. The wires themselves were potted securely in the milled grooves using epoxy and were prevented from vibrating loose from these grooves by the next adjacent layer of cooling channels, since all layers were tightly sandwiched together.

Coil Construction

To produce high gradient efficiencies, it is advantageous to use the maximum number of wires possible. This number is constrained in an obvious way by the wire diameter, minimum spacing between wires, and circumference of the cylindrical former. To obtain the desired gradient efficiencies for these coils, it was necessary to use relatively small wires (AWG no. 20) with a diameter of ~1 mm and an interwire spacing of 0.5 mm. The G_x (outermost) coil was wound with a single length of wire such that 216 axially directed segments generated the required current density, and for the G_z (innermost) coil, 200 axially directed segments were wound. For the middle coil (G_y), constraining the closest separation of the wires to be 0.5 mm allowed 48 loops per side. For all three coils, the wire paths were milled (numerically controlled) into the surface of polycarbonate/acrylic formers. Wire was then wound into these grooves and epoxied in place. Figure 4a shows the constructed G_x coil, complete with horizontal plates after winding with (dielectric) insulated copper wire. The upper plates were curved downward at the superior and inferior ends to provide a more comfortable structure for patient support. Figure 4b shows the middle coil (G_y) before assembly of the complete gradient coil unit.

The resistivity of the small-diameter wire used to construct the coils is relatively high, increasing from 33.3 mΩ/m at room temperature to 40.5 mΩ/m at 75°C (our specified upper limit on temperature at the wire). The additional length of wire required to extend the return paths away from the main cylinders also contributed to high coil total resistances. Since high root-mean-squared (RMS) currents are required for the desired imaging applications, the power dissipated by the coils is significant (~1250 W for one coil @ 25A RMS). In a mock-up of one quadrant of a coil, when a 25A RMS current was applied

with no cooling, the temperature of the quadrant rose from 10°C to 100°C in 2.5 minutes. With air cooling only, a temperature rise from 10°C to 35°C in 4 minutes was observed. A more efficient cooling system was therefore required to ensure patient safety.

Water is one of the most efficient and economical cooling fluids available. Its heat capacity (C_p = 4.18 J/g/°C) is approximately two times higher than other commonly available cooling fluids such as hydrocarbon oils (e.g., ethylene glycol). Assuming that all heat generated is transferred to the cooling water and the maximum allowable temperature rise of the water is 5°C, a water flow of 3.6 liter/min is required to remove 1250 W of heat. Conventionally, water-cooling channels for gradient coils are constructed from copper tubing. For a compact gradient coil set, the competing demands of space limitations and the requirement of a large cooling channel cross-section to ensure adequate volume flow rates necessitated the design of a novel cooling system. We designed this cooling system in separate modules, each module corresponding to a quadrant of a single gradient coil. Each module consisted of a skeleton of cooling channel spacers that were milled from a 3.0-mm-thick polycarbonate sheet. This was covered on both sides with a very thin (0.25-mm-thick) polycarbonate film (GE Plastics, General Electric Company, Pittsfield, MA) to allow close thermal contact of the wires with the cooling water while ensuring electrical insulation. The film was bonded to the skeleton using ultraviolet-curing polyvinyl chloride-based bonding adhesive (Loctite 3311, Loctite Corporation, Mississauga, Canada). The tensile strength (to break) of the polycarbonate film was rated at 9000 psi, according to American Standards of Testing Materials (ASTM) D882, and the burst strength was 200 psi (ASTM D774). The modules were tested for flow uniformity and resistance to leaks by flowing water at 13 liter/min for >5 hours before permanent incorporation into the gradient coil structure. After incorporation into the gradient coil set, the modules were connected in parallel to lower the fluid resistance of the network of cooling channels and thereby allow increased water flow rates.

This design allowed very close thermal contact between the wires and water in the cooling channels (while maintaining electrical isolation) and also provided a large surface area over which heat could be transferred to the water. The ability to test the cooling channel integrity separate from the gradient coil structure was vital in ensuring no electrical shorting due to water leakage. An additional benefit of constructing the cooling system from polycarbonate is that no electrical currents can be created in this material, and it is therefore not susceptible to eddy current generation like some copper systems. Since the thickness of the cooling channel module was only 3.5 mm, the maximum total wall thickness of the gradient coil structure was less than 3 cm. The assembled gradient coil structure, including RF coil and water connections, is shown in Fig. 5.

RF Coil

Several cylindrical RF coil designs exist that can be used in a transverse geometry for imaging the breast (i.e., with
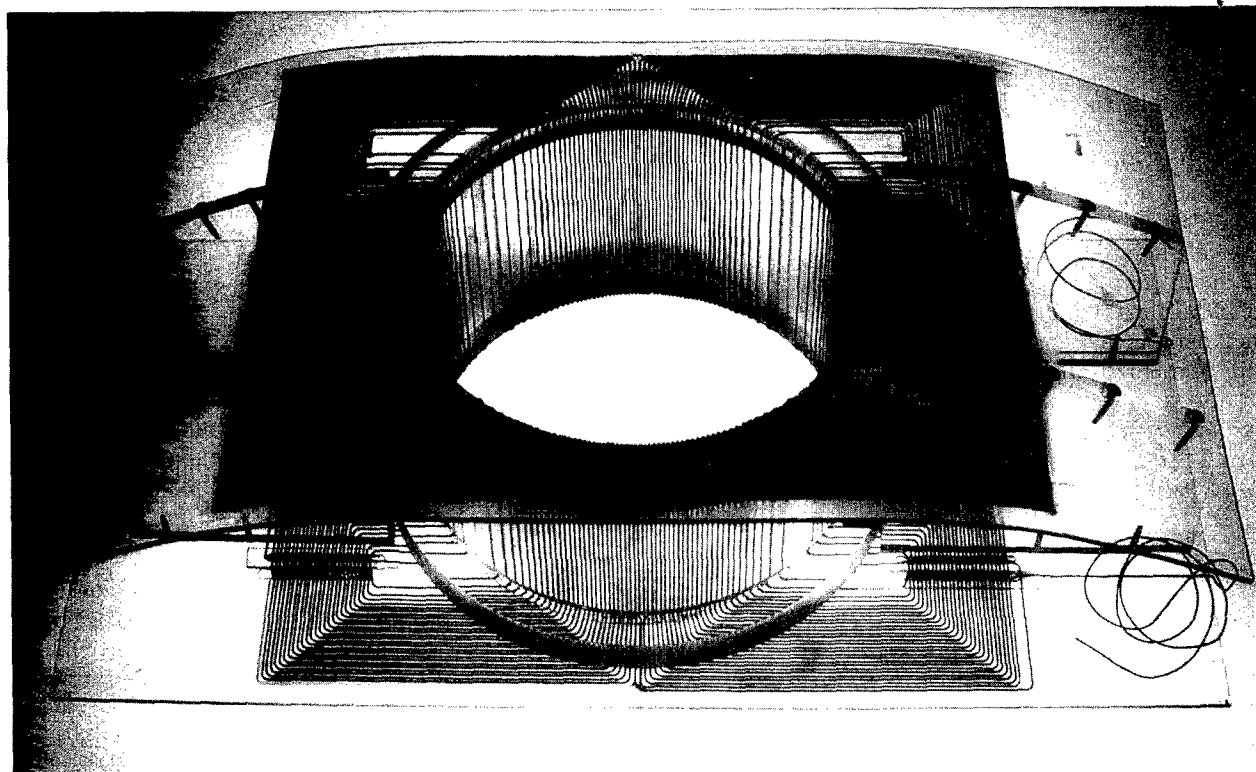
a
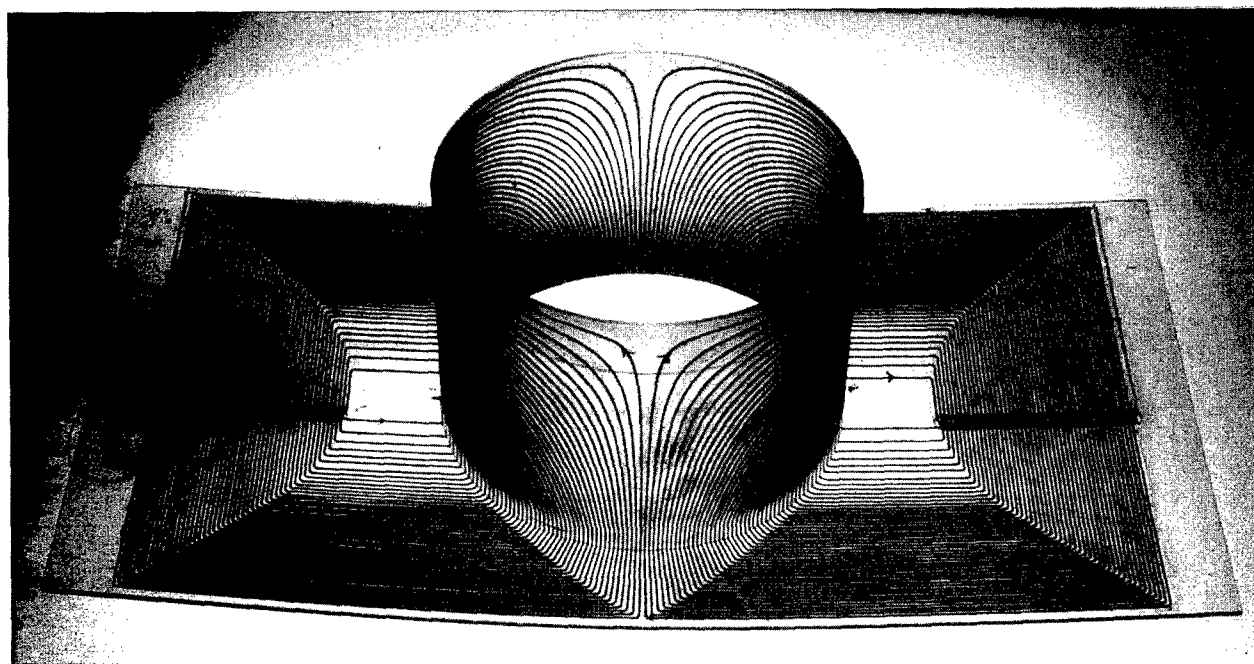
b

FIG. 4. (a) G_x quadrupole coil with 216 windings. (b) G_y coil showing placement of the "return wires" on a horizontal plate.

the coil axis perpendicular to the main magnetic field B_o). These coils, when oriented vertically, produce B_1 fields directed along either the horizontal x direction (e.g., saddle coils (6)) or along the vertical direction (e.g., solenoidal coils (7, 8)).

The construction of an RF coil for operation inside our breast gradient coils is a difficult problem, in that the proximity of the RF coil to the gradient coils results in very strong inductive coupling and detuning of the RF coil (given that the gradient coil radius is constrained to be as small as possible for maximum efficiency). To determine the best RF coil design for our gradient coil set, two different RF coils were constructed and tested. The first coil constructed was a quadrature RF coil with

FIG. 5. Assembled gradient coil module showing RF coil and cooling channels.

two separate coils providing the perpendicular B_1 components. In this arrangement, a simple three-loop solenoidal coil provided the vertical mode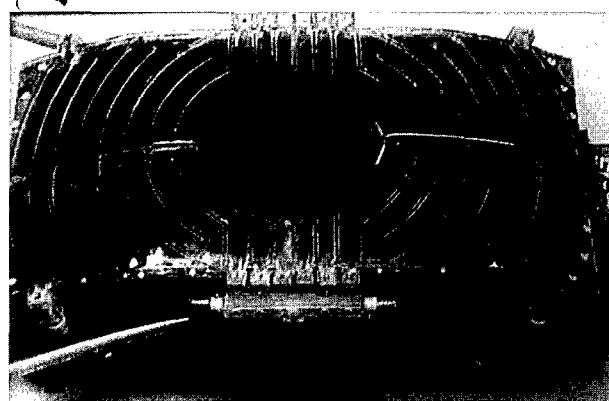, and a saddle coil built onto the same former provided the horizontal mode. The second coil constructed was a 16-rung high-pass birdcage RF coil designed for operation in a linear mode (recall that a birdcage coil cannot be used in quadrature mode in the vertical orientation because one of the modes would be parallel to B_0). We chose this design over a saddle-coil arrangement because of the superior uniformity of B_1 produced by the birdcage coil over the volume enclosed by the coil. A split cylindrical RF shield was constructed from fine copper screen and located immediately inside the smallest diameter gradient coil. The coils were tested for coupling to the gradient coils. The quality factors, Q, were measured, and the coil performances were compared.

Diffusion Imaging

Preliminary diffusion measurements were made using a short-T_2 phantom consisting of $NiSO_4$-doped agarose gel ($T_2 = 60$ ms at 1.89 T) with a diffusion-sensitized spin-echo sequence (pulsed gradient spin-echo sequence (9)). Apparent diffusion coefficient (ADC) maps were calculated from a series of 10 diffusion-weighted images with diffusion b factors between 0 and 1000 s/mm². Each of these images was the geometrical average of two images with equal diffusion-weighting but with opposite diffusion gradient polarity to remove the effects of diffusion-weighting cross-terms from interaction between the diffusion and imaging gradients (10). The ADC maps were obtained under three conditions: (1) using the standard whole-body manufacturer-supplied gradient coils for all imaging and diffusion-weighting gradients; (2) using our custom coils for all imaging and diffusion-weighting gradients, with the gradient strengths matched to those of the whole-body coils by applying an appropriately scaled current to the coils; and (3) using our custom coils for all imaging and diffusion-weighting gradients, with the imaging gradient strengths matched to those of the whole-body coils, but taking advantage of the increased gradient efficiency to apply higher strength, shorter diffusion-weighting gradients, thereby shortening the scan TE. In the first two experiments, the minimum TE required for

diffusion weighting of $b = 995$ s/mm² was TE = 80 ms (with diffusion gradient strength of 22 mT/m). TR was set to 600 ms, the matrix size for the scan was 256×128, and the image size was 8×8 cm, for a total scan time of 2.5 minutes for each image (5 minutes for each b factor). Diffusion gradients were applied along the readout axis, x, for all experiments. For the third experiment, the TE was decreased to TE = 46 ms by increasing the strength of the diffusion-weighting gradient pulses by a factor of four (88 mT/m) to obtain much larger b factors with shorter diffusion pulses. All other parameters (including slice thickness) were matched to the first two experiments.

RESULTS

Coil Performance

The field produced by each of the three coils was calculated by direct numerical solution of the Biot-Savart Law for the wire paths, including return wire contributions. Calculated gradient efficiency for all three coils, together with the measured resistance and inductance, are summarized in Table 1. Contour plots of calculated gradient uniformity for the G_z quadrupole coil are shown in Fig. 6. Figure 6a shows the percentage deviation from gradient uniformity for a y-x plane through the center of the coils. A similar plot is shown in Fig. 6b for a x-z plane, transverse to the coil axis, at a height equal to the center of the VOI (i.e., located 5.9 cm below the top surface of the coils). These plots show the excellent gradient uniformity within the VOI that is predicted for the G_z coil. The gradient strength decreases near the ends of the coil, because the finite length of the coil causes a decrease in field strength. Similar results were obtained for the G_x gradient coil, with appropriate scaling for the number of wires and the coil radius. The performance of the modified target field G_y coil is shown in Figs. 6c and 6d. A larger deviation from gradient uniformity is present for this coil, compared to the G_x and G_z coils. This problem is inherent to any design for a G_y coil in the transverse orientation, since there is an additional gradient in the y direction due to the natural field fall-off that occurs as the ends of the coil are approached. To create a G_y coil with optimum gradient efficiency, we would like to maximize $|B_z|$ at both ends of the coil, with B_z a maximum in the $+z$ direction at one end of the coil, and a maximum in the $-z$ direction at the opposite coil end. The field fall-off inherent in this coil orientation works against the gradient we desire to create, since it necessarily results in a decrease in the magnitude of B_z as the coil ends are approached. Instead of working against the natural field fall-off toward the ends of the coil, we have designed a

Table 1
Coil Performance Characteristics

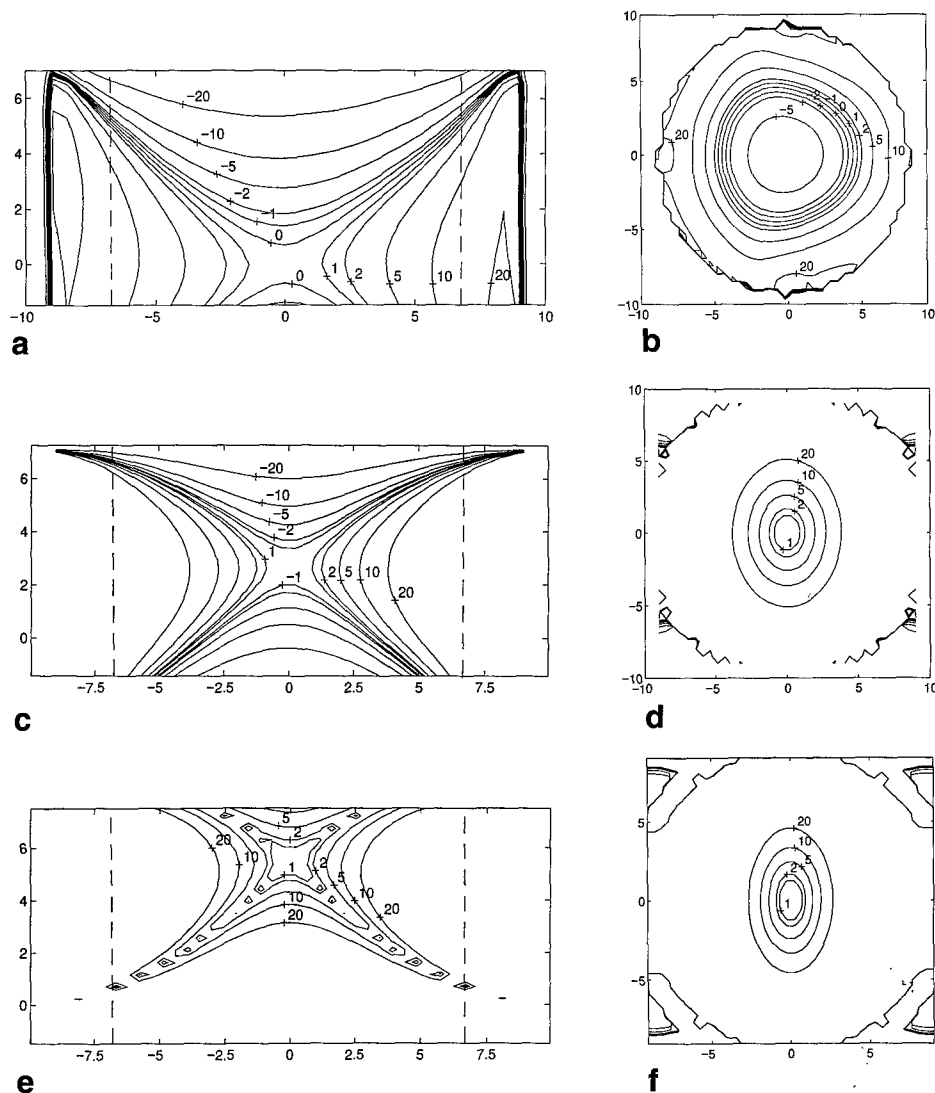|	Mean diameter (cm)	Efficiency (mT/m/A)	Inductance (μH)	Resistance (Ω)
G_x (quadrupole)	21.1	2.9	754	2.3
G_y (fingerprint)	19.5	1.7	829	2.6
G_z (quadrupole)	18.1	3.3	1024	1.9

FIG. 6. Contour plots showing percentage deviations from gradient uniformity for the G_z coil over (a) an axial plane (x-y) showing the entire VOI with the top edge of the plot corresponding to the top surface of the coils. The outer circumference of the VOI is at 6.75 cm, as indicated by dashed lines. (b) A coronal plane (x-z) located at the center of the defined VOI, i.e., at ~3 cm above the geometric coil center. In Fig. 6a, the contours are symmetric around $y = 0$ cm with some small deviations due to return-wire contributions. (c, d) The corresponding plots for the constructed G_y coil shown in Fig. 4b. (e, f) The corresponding plots for a conventional transverse coil with return wires on the cylinder, as in Fig. 3b.

coil to produce $B_z = 0$ at the upper end of the coil, and a maximum in B_z toward the bottom end, similar to the asymmetric head coil design by Roemer (11). We used the target field approach to optimize the rate at which the field falls off toward the upper end of the coil to produce a linear variation in B_z. Although the region of acceptable gradient uniformity for our truncated target field coil is not as large as for the quadrupole coils, it compares favorably to the performance of the full target field design. We show in Figs. 6e and 6f the corresponding plots from a complete 40 loop per side target field coil with the same dimensions as our modified coil (i.e., with return wire paths at the bottom of the cylinder as in Fig. 3b). The region of acceptable gradient uniformity for our truncated target field coil is much larger than for the complete target field coil. In addition, the gradient efficiency is better for our truncated coil by a factor of 1.7, due to

the larger number of windings that could be placed on the cylinder for our coil.

To verify the field simulations, gradient uniformity was tested by acquiring images of grid phantoms. Deviations from gradient uniformity are manifest in the images as geometric distortions. The phantoms consisted of acrylic cylinders filled with square plastic gridding and $CuSO_4$-doped 0.9% saline solution. The grid spacing was 1.7×1.7 cm, whereas the phantoms had an outer diameter of 12.5 cm and a height of 15 cm (extending 3 cm higher than the top surface when placed inside the coils). The coil performance was tested on a clinical GE Signa imager, using our coils for all imaging gradients (with gradient strengths matched to the whole-body coils) in a standard spin-echo pulse sequence. In general, local gradient coils often require modification of the compensation network for the gradient coil amplifiers since the

coil inductances are quite different from the whole-body coils. Because the inductances of our breast coils were very similar to the whole-body coils, no modification of the network was necessary. Images of a grid phantom are shown in Fig. 7 for planes corresponding approximately to the theoretical field plots shown in Figs. 6a and 6b and are evidence of the good gradient uniformity achieved over most of the VOI. These images were acquired using a spin-echo sequence with TE = 20 ms, TR = 500 ms, matrix size = 256 × 256, and 2 NEX. The image size is 16 × 16 cm, and the VOI vertical extent is marked with arrows.

The first RF coil we constructed was a quadrature coil consisting of a solenoidal coil to provide the vertical mode and a saddle coil to provide the horizontal coil. Unfortunately, the vertical mode was inductively coupled to both the y-gradient coil and to the RF shield and could not be tuned to the proton resonant frequency at 1.5 T. We therefore chose to construct a coil that would operate in linear mode, with only a horizontal B_1 component present. We constructed a birdcage coil that creates a horizontal mode B_1 field with a high degree of homogeneity over a large volume. The unloaded Q of this coil (when located inside the gradient coil structure) was 80, whereas the Q for loading with a 0.9% saline phantom was 29.

Although the gradient strengths required for conventional imaging (10 mT/m) can be generated at less than 6 A using these coils, higher currents are required for more demanding applications such as flow imaging and diffusion imaging. To test the effectiveness of the water cooling system, a DC current was applied to the coil with the highest total resistance, G_y, and the temperature rise was measured for different water flow rates by monitoring a thermocouple located on the surface of the wires. The temperature was monitored until equilibrium was achieved. Measured temperature rises are shown in Fig. 8 for DC currents between 0 and 22 A and a cooling water flow rate of 8 liter/min. Similar results were obtained for other flow rates, at which the equilibrium temperature increased with decreasing flow rates but did not change significantly from the results shown in Fig. 8 for higher flow rates. This behavior has also been demonstrated in purely cylindrical gradient coils and was modeled by Chu and Rutt (12) using an analysis based on fundamental heat transfer theory.

Diffusion Imaging

ADC maps for a T_2 = 60 ms NiSO$_4$-doped agar phantom are shown in Fig. 9; Fig. 9a shows the results obtained using the GE gradient coils, and Fig. 9b shows the results obtained using our gradient coils with diffusion gradient strengths four times higher than that of the GE coils. The mean ADC for all three experiments was the same within experimental error: $(1.8 \pm 0.3) \times 10^{-3}$ mm^2/s for the GE coils ($\pm 30\%$ peak-to-peak), $(1.8 \pm 0.3) \times 10^{-3}$ mm^2/s for our gradient coils with diffusion gradient strengths matched to the GE coils, $(1.9 \pm 0.2) \times 10^{-3}$ mm^2/s for our gradient coils with diffusion gradient strengths four times higher than that of the GE coils and TE = 46 ms. As expected, the observed signal-to-noise ratio was increased by nearly a factor of 2 for the TE = 46 ms images compared to the corresponding b-factor images at TE = 80 ms.

DISCUSSION

The performance and homogeneity of the gradient coils were in excellent agreement with theoretical predictions. The volume of acceptable gradient uniformity (<20% deviation) extended over most of our defined VOI for all
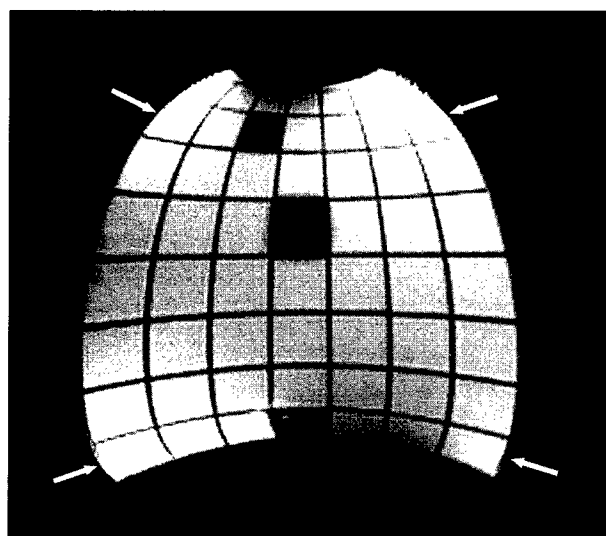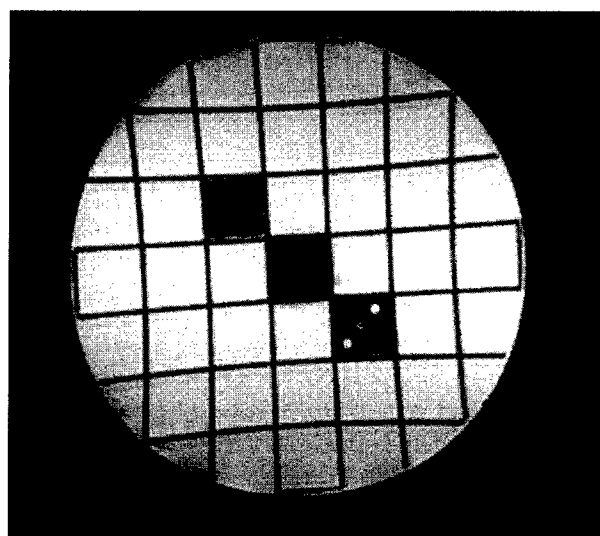
a   **b**

FIG. 7. Spin-echo images of a grid phantom acquired (a) for an axial plane (x-y) and (b) for a coronal plane (x-z) with the specialized breast quadrupole gradient coils. The input current strength required for the least efficient (G_y) coil was approximately 14 times less than that required for the corresponding GE coil.

FIG. 8. Temperature response of assembled gradient coils to a DC current applied to the coil with the highest resistance (G_y) monitored at the surface of the G_y coil where the winding density was greatest.

three gradient coils. For this region, the theoretical plots of B_z can be used to generate a gradient-warping algorithm for the coils (13) to correct spatial distortions in the images. Additio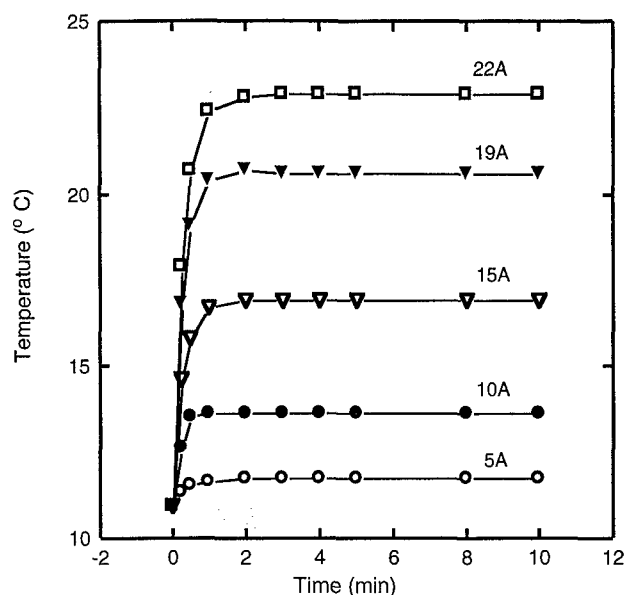nally, the known deviations from gradient uniformity can be used to correct calculations of diffusion-weighting b factors (which will vary spatially across the VOI for our coils). Unfortunately, greater deviations from uniformity could not be avoided for the top 1 cm of the VOI near the upper edges of the coils for our coil designs. Deviations from uniformity of more than 20% lead to large image distortions and likely cannot be satisfactorily corrected using conventional schemes. Many breast lesions occur close to the chest wall; to be clinically useful, it is important to image accurately as close to the chest wall as possible. Several new gradient coils with improved gradient uniformity at the top edge of the coil have been reported recently (14, 15). Future improvements on our coil design will focus on extending the region of usable gradient beyond the top edge of the coil (16) as far as possible. For our preliminary clinical work with these coils, we will limit our study to patients with known lesions occurring in a region of the breast that falls within the 20% uniformity region of our gradient coils. This approach will allow us to implement pulse sequences under ideal conditions, (a) to determine the best parameters for visualizing breast lesions, (b) to determine the minimum required gradient strengths and uniformities, and (c) to make an initial assessment of the clinical utility of this approach.

In future coil designs, it may be possible to extend the region of usable gradient farther into the cylinder in the $-y$ direction by recessing the coils in the patient table or by constructing a dedicated breast imaging table, thereby allowing higher aspect ratio coils. In this design, the coil assembly would be constructed to allow positioning on either side of the table, depending on which breast was being imaged. A fiberglass or Kevlar sheath covering the coil assembly and running the length of the patient table would serve the dual functions of isolating the patient from the electrical and cooling circuits and providing an additional form of mechanical fixation to secure the coils on the table. Because the coils are not torque-balanced, it will be necessary to anchor the structure firmly, both from the point of view of vibration-induced imaging artifacts and of patient safety.

The high gradient efficiencies of these coils will allow much higher spatial-resolution imaging than can currently be achieved in a clinical setting, and additionally, will provide very large amplitude motion-sensitizing gradients, thus facilitating diffusion imaging (or flow imaging) in small blood vessels with short echo times. T_2 has been measured for human breast tissue, with reported values ranging between 60 and 150 ms (17, 18). Recently, we reported T_2 approximately 70 ms for human breast tumor (MCF7 human breast carcinoma) growing in a mouse mammary fat pad (19). More fibrous tumors can have significantly shorter T_2s. For this reason, initial signal loss at $b = 0$ s/mm^2 due to T_2 weighting of the image can severely limit the range of b factors for which images can be obtained, which has the result of limiting the precision of the ADC measurement. Our approach is to shorten TE while maintaining diffusion weighting by increasing diffusion gradient amplitudes. This gives a substantial increase in initial signal intensity for $b = 0$ s/mm^2, allowing high-quality images to be obtained for much higher b factors. Even in cases in which signal loss from T_2 weighting is not so severe as to limit ADC precision, the ability to obtain high diffusion weighting with short TE reduces dramatically the T_2 contrast in an image. This will allow acquisition of a diffusion-weighted image in which the contrast is determined mainly by tissue ADC rather than by a mix of ADC and T_2.

A secondary important benefit that can be gained using high-efficiency gradient coils is that the ramp time required to attain imaging gradient strengths (10–25 mT/m) is decreased from that required by whole-body coils by a factor of the efficiency (since the current slew rate is similar to whole-body coils, and the required peak current is decreased). This will enable echo-planar imaging (and other fast imaging techniques) using conventional gradient amplifiers. Echo-planar imaging techniques have been proven to be much less susceptible to motion artifacts than conventional imaging sequences (20) and have recently been applied to diffusion imaging *in vivo* (21) with good results.

For rapid imaging pulse sequences, and for high-amplitude bipolar pulses, very rapid changes in gradient polarity are required. Although the magnetic field amplitudes drop off quickly in the region above the coils, magnetic fields are also generated by the return wires on the horizontal plate, and excitation thresholds for cardiac stimulation must be considered. As an upper limit for one coil, $|B|$ was calculated for the G_z coil at various distances above the return wires at the location of the highest wire density. The maximum dI/dt from our gradient coil amplifiers is 200 A in 184 μs. This produces dB/dt = 156 T/s at 1 cm above the coil return wire plate
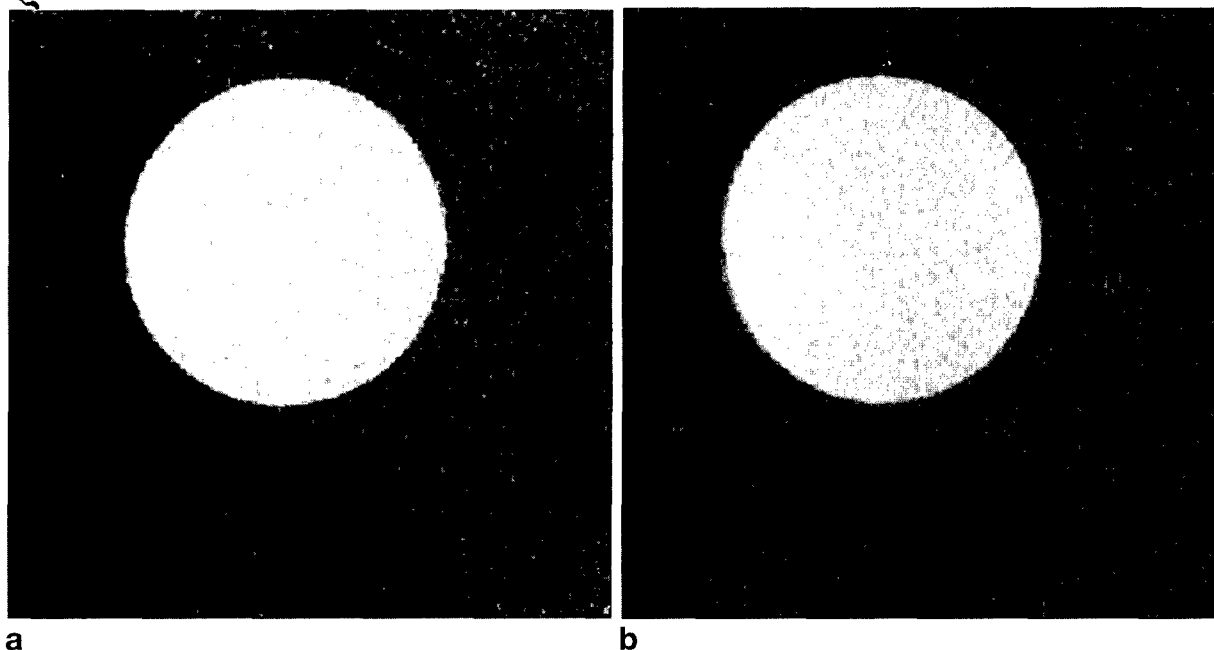
FIG. 9. ADC maps of a T_2 = 60 ms agar phantom obtained (a) using the whole-body coils to provide all diffusion and imaging gradients, TE = 80 ms, and (b) using the breast gradient coils to provide all gradients, where the diffusion gradient strengths were four times the whole-body gradient strengths and TE = 46 ms. In all cases, the ADC maps were constructed from 10 images with b = 0 to b = 1000 s/mm².

and dB/dt = 50 T/s at 10 cm, compared to a recommended upper limit of 400 T/s for cardiac stimulation (22). The magnitude of these fields is relatively small at regions of concern with respect to magnetic stimulation such as the heart; however, peripheral nerve stimulation has been reported at dB/dt as low as 40 T/s in some patients (22). Theoretical field calculations will allow prediction of $|B|$ and dB/dt for all pulse sequences before implementation, and pulse sequences will be tailored to adhere to maximum dB/dt and peak $|B|$ guidelines. Additionally, if peripheral nerve stimulation is reported for individual patients, dB/dt will be reduced below the stimulation threshold by increasing gradient switching times.

SUMMARY

We have constructed a three-axis gradient coil set for imaging human breast tumors. These coils create gradient efficiencies of up to 3.3 mT/m/A with relatively low inductance (≤1000 μH), and good gradient uniformity over most of the volume required for breast imaging. Preliminary diffusion results were obtained in a water phantom for b factors as high as ~1000 s/mm² for TE = 46 ms. A compact, efficient water-cooling system was presented, which maintained coil temperatures at or below room temperature, even for RMS currents as high as 20 A. This gradient/cooling module will allow, for the first time, clinical breast imaging using diffusion and microvascular flow-weighted protocols with high spatial resolution.

REFERENCES

1. D. S. Webster, K. H. Marsden, Improved apparatus for the NMR measurement of self- diffusion coefficients using pulsed field gradients. *Rev. Sci. Instrum.* **45,** 1232–1234 (1974).
2. K. C. Chu, B. K. Rutt, Quadrupole gradient coil design and optimization: a printed circuit board approach. *Magn. Reson. Med.* **31,** 652–659 (1994).
3. W. G. O'Dell, J. S. Schoeniger, S. J. Blackband, E. R. McVeigh, A modified quadrupole gradient set for use in high resolution MRI tagging. *Magn. Reson. Med.* **32,** 246–250 (1994).
4. R. Turner, A target field approach to optimal coil design. *J. Phys. D. Appl. Phys.* **19,** L147–151 (1986).
5. R. Turner, Gradient coil design: a review of methods. *Magn. Reson. Med.* **11,** 903–920 (1993).
6. P. W. McOwan, T. W. Redpath, A specialised receiver coil for NMR imaging of female breasts. *Phys. Med. Biol.* **32,** 259–263 (1987).
7. J. P. Hornak, J. Szumowski, R. G. Bryant, Elementary single turn solenoids used as the transmitter and receiver in MRI. *Magn. Reson. Imaging* **5,** 233–237 (1987).
8. L. Sun, L. O. Olsen, P. L. Robitaille, Design and optimization of a breast coil for magnetic resonance imaging. *Magn. Reson. Imaging* **11,** 73–80 (1993).
9. E. O. Stejskal, J. E. Tanner, Spin diffusion measurements: spin echoes in the presence of a time-dependent field gradient. *J. Chem. Phys.* **42,** 288–292 (1965).
10. M. Neeman, J. P. Freyer, L. O. Sillerud, A simple method for obtaining cross-term-free images for diffusion anisotropy studies in NMR microimaging. *Magn. Reson. Med.* **21,** 138–143 (1991).
11. P. B. Roemer, Transverse gradient coils for imaging the head. United States Patent No. 5177442, January 5, 1993.
12. K. C. Chu, B. K. Rutt, MR gradient coil heat dissipation. *Magn. Reson. Med.* **34,** 125–132 (1995).
13. M. O'Donnell, W. A. Edelstein, NMR imaging in the presence of magnetic field inhomogeneities and gradient field nonlinearities. *Med. Phys.* **12,** 20–26 (1985).
14. A. Ersahin, H. K. Lee, O. Nalcioglu, Asymmetric gradient coil design for high resolution breast imaging, in "Proc., SMR and ESMRMB, 3rd

Annual Meeting, Nice, 1995," p. 954.

15. H. K. Lee, R. Raman, R. Slates, A. Ersahin, O. Nalcioglu, An optimized gradient coil for breast imaging, *in* "Proc., SMR and ESMRMB, 3rd Annual Meeting, Nice, 1995," p. 955.

16. B. A. Chronik, B. K. Rutt, Constrained length minimum inductance gradient coil design, *in* "Proc., ISMRM, 5th Annual Meeting, Vancouver, B.C., Canada, 1997," p. 53.

17. D. Z. J. Chu, W. S. Yamanashi, J. Frazer, C. F. Hazlewood, H. S. Gallager, A. W. Boddie, R. G. Martin, Proton NMR of human breast tumors: correlation with clinical prognostic parameters. *J. Surg. Oncol.* **36**, 1–4 (1987).

18. S. J. Graham, M. J. Bronskill, J. W. Byng, M. J. Yaffe, N. F. Boyd, Quantitative correlation of breast tissue parameters using MR and X-ray mammography. *Br. J. Cancer* **73**, 162–168 (1996).

19. C. F. Maier, Y. Paran, P. Bendel, B. K. Rutt, H. Degani, Quantitative diffusion imaging in implanted human breast tumors. *Magn. Reson. Med.* **37**, 576–581 (1997).

20. R. Turner, D. LeBihan, Single-shot diffusion imaging at 2.0 Tesla. *J. Magn. Reson.* **86**, 445–452 (1990).

21. R. Turner, D. LeBihan, A. S. Chesnick, Echo-planar imaging of diffusion and perfusion. *Magn. Reson. Med.* **19**, 247–253 (1991).

22. J. P. Reilly, Principles of nerve and heart excitation by time-varying magnetic fields, *in* "Biological effects and safety aspects of NMRI and spectroscopy." *Ann. N. Y. Acad. Sci.* **649**, 96–107 (1993).

Constrained Length Minimum Inductance Gradient Coil Design

Blaine A. Chronik, Brian K. Rutt

A gradient coil design algorithm capable of controlling the position of the homogeneous region of interest (ROI) with respect to the current-carrying wires is required for many advanced imaging and spectroscopy applications. A modified minimum inductance target field method that allows the placement of a set of constraints on the final current density is presented. This constrained current minimum inductance method is derived in the context of previous target field methods. Complete details are shown and all equations required for implementation of the algorithm are given. The method has been implemented on computer and applied to the design of both a 1:1 aspect ratio (length:diameter) central ROI and a 2:1 aspect ratio edge ROI gradient coil. The 1:1 design demonstrates that a general analytic method can be used to easily obtain very short gradient coil designs for use with specialized magnet systems. The edge gradient design demonstrates that designs that allow imaging of the neck region with a head-sized gradient coil can be obtained, as well as other applications requiring edge-of-cylinder regions of uniformity.

Key words: gradient coils; target field; current constraints; minimum inductance; constrained length.

INTRODUCTION

Advanced MR imaging and spectroscopy methods often require high performance gradient hardware, where performance is typically characterized by a combination of gradient efficiency (gradient strength per unit current) and switching speed. The design of gradient coils customized to a particular application is a method of realizing gains in both. One defining characteristic of customized gradient coils is that they conform closely to the anatomical region of interest and although this allows increased performance, subject access to the usable region of the coil becomes an important and nontrivial design consideration.

Gradient coil design methods can be divided into two general categories: "coil space" versus "reciprocal space" techniques. Coil space methods iteratively adjust the positions of wires on the gradient coil former until the design conforms to some desired performance specifications. The optimal wire configuration is chosen, using a numerical optimization technique, from the multitude of

wire configurations that span the domain of allowable patterns. The method of Conjugate Gradient Descent (1, 2) and the method of Simulated Annealing (3–6) are examples of different optimization techniques applied to this problem. Although these methods in principle allow complete freedom in the wire pattern and can be applied to any geometry, they are in practice limited due to the computational intensity of the methods. They have been most effectively applied to the problem of positioning coaxial circular wire loops in the design of longitudinal (G_z) gradient coils; furthermore, when applied to the design of cylindrical transverse gradient coils $(G_x$ or $G_y)$, the functional form of the wire shapes have typically been predetermined to depend on only a few parameters so that the number of degrees of freedom remains practical. Advantages of these methods include the absence of an approximation stage in sampling a continuous current density with a finite number of wires, and most importantly the ease with which they incorporate direct constraints on the final wire pattern, thereby allowing the design of restricted length gradient coils. The first advantage is primarily of concern only when the current density is to be sampled with a small number of wires, since field variations due to finite wire spacing become insignificant at distances larger than that spacing.

Reciprocal space methods are characterized by the expansion of all quantities of interest in terms of orthogonal functions and solving for the coefficients of the corresponding current density expansion. The current density is then approximated by a finite set of wires, typically using stream function methods (7). Because of the difficulty in obtaining orthogonal function expansions for general geometries, in practice these techniques are limited to simple geometries (planes (8, 9), cylinders (10, 11), spheres (12), ellipses (13), hyperbolas (14)); furthermore, they often lack control over the final current density that is attainable with coil space methods (15). Once quantities of interest have been expanded and the coefficients of the current density expansion formally solved for, computer implementation of these methods is simple and current densities can be obtained very quickly. Reciprocal space methods can yield optimal designs by using constrained Lagrange multiplier or least squared error methods to solve for the expansion coefficients (16).

In this paper we address the problem of including direct control over current density in a reciprocal space design method. We present the details of a modification of Turner's minimum inductance target field method (17) that allows explicit constraint of the extent of the final current density as well as control over the position of the uniform gradient with respect to the current density while minimizing coil inductance. These modifications yield a design method with the generality claimed for

coil space methods and the efficiency of reciprocal space techniques.

THEORY

In any magnetic design problem the most important step is the establishment of a relationship between the current density function and the desired magnetic field components. For gradient coils used in MRI, we are only concerned with the z-component of the magnetic field, $B_z(r, \phi, z)$; furthermore, if we are considering axially aligned cylindrical gradient coils (define the coil axis to lie along the z direction), only the azimuthal component of current density, $J_\phi(\phi, z)$, contributes to $B_z(r, \phi, z)$ and therefore the problem reduces to obtaining the connection between these two quantities. There are several ways to express this relationship but one that has proved especially fruitful is the "target field" formalism first described by Turner (10). This formalism is characterized by the expansion of $B_z(r, \phi, z)$ in cylindrical harmonics (18):

$$B_z(r, \phi, z)$$

$$= (-\mu_o a) \sum_{m=-\infty}^{\infty} \int_{-\infty}^{\infty} dk e^{im\phi} e^{i2\pi kz} |k| I_m(|2\pi kr|) \quad [1]$$

$$K'_m(|2\pi ka|) j_\phi^m(k)$$

where I_m and K_m are modified Bessel functions, a is the radius of the cylinder on which the current is constrained to flow, and

$$j_\phi^m(k) = \int_{-\pi}^{+\pi} d\phi \ e^{-im\phi} \int_{-\infty}^{+\infty} dz \ e^{-i2\pi kz} J_\phi(\phi, z) \quad [2]$$

is the 2D Fourier Transform of $J_\phi(\phi, z)$ in cylindrical coordinates. All target field based methods express quantities of interest as functions of $j_\phi^m(k)$ and then directly solve for the $j_\phi^m(k)$ that yields the desired gradient coil. Methods only differ in terms of the physical quantities explicitly included in the design process and how the required $j_\phi^m(k)$ is solved for. It should be emphasized that all target field methods are direct inverse solutions to the gradient coil design problem and that once $j_\phi^m(k)$ is known, the current density obtained via inverse transformation of $j_\phi^m(k)$ will give the desired gradient coil, i.e., one which produces exactly the specified field.

"Original" Target Field

The original target field method developed by Turner (10) makes use of the fact that the 2D Fourier transform of $B_z(r, \phi, z)$ is very simply related to $j_\phi^m(k)$:

$$B_z^m(c, k) = \omega^m(c, k) j_\phi^m(k) \quad [3]$$

where

$$\omega^m(c, k) = (-\mu_o a)|k| I_m(|2\pi kc|) K'_m(|2\pi ka|) \quad [4]$$

and

$$B_z^m(c, k) = \int_{-\pi}^{+\pi} d\phi \ e^{-im\phi} \int_{-\infty}^{+\infty} dz \ e^{-i2\pi kz} B_z(c, \phi, z) \quad [5]$$

with c the radius of a cylindrical surface ($c < a$), called the "target cylinder." It is useful to think of $B_z^m(c, k)$ as an apodised version of $j_\phi^m(k)$, and $\omega^m(c, k)$ acting as the apodising function with limiting forms:

$$\omega^m(c, k) \sim e^{-2\pi k(a-c)}; \quad k \to \infty \quad [6a]$$

$$\omega^m(c, k = 0) = \frac{\mu_o c}{4\pi a} \quad [6b]$$

Knowing that $B_z^m(c, k)$ and $j_\phi^m(k)$ are related via a simple product translates into a convolution relationship between $B_z(c, \phi, z)$ and $J_\phi(\phi, z)$:

$$B_z(c, \phi, z) = \Omega(c, z) \otimes J_\phi(\phi, z) \quad [7]$$

where $\Omega(c, z)$ is the inverse transform of $\omega^m(c, k)$. $\Omega(c, z)$ is approximately Lorentzian in shape with full width at half-maximum proportional to (a-c); this means that the magnetic field has the same functional form as the azimuthal current density but "smeared" in the z direction by a Lorentzian-like function that gets broader as the target cylinder moves further away from the current-carrying cylinder. In other words, the longitudinal component of magnetic field is a "low-pass filtered" version of the azimuthal component of current density.

To obtain a gradient coil, the desired field on the target cylinder must be specified (i.e., the "target field"). Generally, we write:

$$B_z(c, \phi, z) = g(z) f(c, \phi) \quad [8]$$

where $g(z)$ is the field modulation along the z direction and $f(c, \phi)$ describes the radial and azimuthal variation of B_z. For longitudinal (G_z) gradient coils we would have $f(c, \phi)$ = constant and the regions of uniform gradient correspond to regions over which the first derivative of $g(z)$ is approximately constant. For transverse gradient coils (G_x or G_y) we would have:

$$f(c, \phi) = cG_x \cos \phi \quad [G_x] \quad [9a]$$

$$f(c, \phi) = cG_y \sin \phi \quad [G_y] \quad [9b]$$

and regions of uniform gradient correspond to regions over which $g(z)$ is approximately constant.

Taking a G_x coil as an example, we combine Eqs. [8] and [9a], substitute the resulting expression for $B_z^m(c, k)$ into Eq. [3] and solve for $j_\phi^m(k)$ to get:

$$j_\phi^l(k) = \frac{cG_x \pi \cdot \Im\{g(z)\}}{\omega^l(c, k)} \quad [10a]$$

$$j_\phi^m(k) = 0; \quad \text{for} \quad m \neq 1 \quad [10b]$$

where $\Im\{g(z)\}$ is the 1D Fourier transform of $g(z)$. Once $g(z)$ has been specified over all z points, the $j_\phi^l(k)$ func-

tion is easily arrived at using Eq. [10a] and $J_\phi(\phi, z)$ obtained by inverse transformation. The $J_z(\phi, z)$ current density component is obtained from $J_\phi(\phi, z)$ by imposing continuity of $\bar{J}(\phi, z)$ (7, 19). It should be noted that although the forms in this paper are general in that they include the complete range of possible m values, the expressions applied to longitudinal and transverse gradient coils greatly simplify to include only the $m = 0$ and $m = \pm 1$ contributions respectively.

Minimum Inductance Target Field

The minimum inductance target field method represents a rather different and more powerful way of solving for $j_\phi^m(k)$ in that we now determine the $j_\phi^m(k)$ that minimizes some property of the gradient coil (typically inductance or power dissipation) subject to the constraint that B_z be equal to specified values (B_{zn}) at a finite set of coordinates (r_n, ϕ_n, z_n). The result of the analysis is still $j_\phi^m(k)$ (the transform of which gives the required current density) and Eq. [3] still holds; however, $j_\phi^m(k)$ is solved for differently.

To set a context for the extension described in this paper, we review the form of the minimum inductance method, first described by Turner (17). It is an application of the method of constrained optimization using Lagrange multipliers (19). A functional, $U\{j_\phi^m(k)\}$, is formed that includes the function, $F\{j_\phi^m(k)\}$ to be optimized (typically F is either inductance, L, or power dissipation, P, both of which are expressible as functions of the current density) and the field constraint equations multiplied by constants, λ_n, the Lagrange multipliers:

$$U\{j_\phi^m(k)\} = F\{j_\phi^m(k)\} + \sum_n \lambda_n[B_z(r_n, \phi_n, z_n) - B_{zn}] \quad [11]$$

In a manner analogous to the optimization of a function of a single variable, the derivative of U with respect to $j_\phi^m(k)$ is taken and set equal to zero. We then solve that equation for $j_\phi^m(k)$. For the specific case of minimizing coil inductance, we first write L as a function of $j_\phi^m(k)$ (17, 20):

$$L = \left(\frac{-\mu_o a^2}{2\pi I^2}\right) \sum_{m=-\infty}^{+\infty} \int_{-\infty}^{+\infty} \cdot dk$$

$$I'_m(|2\pi ka|) K'_m(|2\pi ka|) j_\phi^m(k)^2 \quad [12]$$

where I is the input current required to produce the surface current density, then note the form of the field constraint equations:

$$B_z(r_n, \phi_n, z_n) - B_{zn} = 0 \quad [13a]$$

$$\left[(-\mu_o a) \sum_{m=-\infty}^{+\infty} \int_{-\infty}^{+\infty} dk e^{im\phi_n} e^{i2\pi kz_n} |k| \right.$$

$$\left. I_m(|2\pi kr_n|) K'_m(|2\pi ka|) j_\phi^m(k) \right] - B_{zn} = 0 \quad [13b]$$

Differentiating U composed of Eqs. [12] and [13b] and solving for $j_\phi^m(k)$ yields:

$$j_\phi^m(k) = \sum_{n=1}^{N} \lambda_n a_n^m(k) \quad [14]$$

$$a_n^m(k) = \left(\frac{-\pi}{a}\right) e^{im\phi_n} e^{i2\pi kz_n} |k| \frac{I_m(|2\pi kr_n|)}{I'_m(|2\pi ka|)} \quad [15]$$

Once the set of λ_n is known, Eqs. [14] and [15] give the required $j_\phi^m(k)$. The λ_n's are determined by substituting $j_\phi^m(k)$ as expressed by Eq. [14] into the N constraint equations of Eq. [13b]. This can be written as a matrix equation for the λ_n's:

$$[M_{11}][\lambda_N] = [B_{zN}] \quad [16]$$

where the elements of matrix M_{11} are known functions of the constraint coordinates and are given as the first row of Table 1. The design algorithm is then simply to choose the N field constraints, calculate the elements of M_{11} from the constraint coordinates and the equations shown in Table 1, solve Eq. [16] for the set of $\{\lambda_n\}$, compose $j_\phi^m(k)$ via Eq. [14] and inverse transform to get $J_\phi(\phi, z)$.

Constrained Current Minimum Inductance Target Field

To add explicit control over the length (and boundaries) of the final current density to the design algorithm, we have modified Turner's minimum inductance method to include a set of current constraints. This type of control over the design is very important when the region of good uniformity is required to be near the extremes of the physical coil, as well as when the total gradient coil length needs to be minimized.

The first form of current constraint that one would want to impose upon a design is a "closure" constraint that prevents any current density from crossing the boundaries of a specified area on the surface of the cylindrical former. This constraint manifests itself in the final coil design as forcing all conducting loops within the specified region to be closed. A simple form of this constraint would be to require that no current density cross the azimuthal lines defined by $\pm z_q$. Analytically this is equivalent to requiring that the integral of $J_\phi(\phi, z)$ on the line along any $\phi = \phi_q$ from $-z_q$ to $+z_q$ be zero:

$$\Lambda(\phi_q, z_q) = \int_{-z_q}^{+z_q} J_\phi(\phi_q, z) dz = 0 \quad [17]$$

For longitudinal gradient coils this constraint does not need to be applied because the z component of current density will always be zero. For transverse gradient coils the azimuthal variation of $J_\phi(\phi, z)$ is always sinusoidal; therefore, the integral constraint only needs to be applied over a single line from $-z_q$ to $+z_q$ (i.e., along constant $\phi = \phi_q$).

The second type of current constraints necessary to force the current density to remain contained within some region of the coil surface are direct constraints on

Table 1
Analytic Forms for the Calculation of Matrix Elements and Subsequent Determination of Lagrange Multipliers in the Constrained Current Minimum Inductance Design Method

$$M_{11}(n, n') = \sum_{m=-\infty}^{+\infty} \int_{-\infty}^{+\infty} dk \Psi_n^m(k) a_{n'}^m(k) = (\pi \mu_o I) \sum_{m=-\infty}^{+\infty} \int_{-\infty}^{+\infty} dk e^{im(\phi_n + \phi_{n'})} e^{i2\pi k(z_n + z_{n'})} |k|^2 \frac{K_m'(|2\pi ka|)}{I_m'(|2\pi ka|)} I_m(|2\pi kr_n|) I_m(|2\pi kr_{n'}|) w^2(k)$$

$$M_{12}(n, p') = \sum_{m=-\infty}^{+\infty} \int_{-\infty}^{+\infty} dk \Psi_n^m(k) b_{p'}^m(k) = \left(-\frac{\pi I}{a}\right) \sum_{m=-\infty}^{+\infty} \int_{-\infty}^{+\infty} dk e^{im(\phi_n + \phi_{p'})} e^{i2\pi k(z_n + z_{p'})} |k| \frac{I_m(|2\pi kr_n|)}{I_m'(|2\pi ka|)} w^2(k)$$

$$M_{13}(n, q') = \sum_{m=-\infty}^{+\infty} \int_{-\infty}^{+\infty} dk \Psi_n^m(k) c_{q'}^m(k) = \left(-\frac{2\pi I}{a} z_{q'}\right) \sum_{m=-\infty}^{+\infty} \int_{-\infty}^{+\infty} dk e^{im(\phi_n + \phi_{q'})} e^{i2\pi kz_n} |k| \text{sinc}(2\pi kz_{q'}) \frac{I_m(|2\pi kr_n|)}{I_m'(|2\pi ka|)} w^2(k)$$

$$M_{22}(p, p') = \sum_{m=-\infty}^{+\infty} \int_{-\infty}^{+\infty} dk \Phi_p^m(k) b_{p'}^m(k) = \left(\frac{\pi I}{\mu_o a^2}\right) \sum_{m=-\infty}^{+\infty} \int_{-\infty}^{+\infty} dk e^{im(\phi_p + \phi_{p'})} e^{i2\pi k(z_p + z_{p'})} \frac{w^2(k)}{I_m'(|2\pi ka|) K_m'(|2\pi ka|)}$$

$$M_{23}(p, q') = \sum_{m=-\infty}^{+\infty} \int_{-\infty}^{+\infty} dk \Phi_n^m(k) c_{q'}^m(k) = \left(\frac{2\pi I}{\mu_o a^2} z_{q'}\right) \sum_{m=-\infty}^{+\infty} \int_{-\infty}^{+\infty} dk e^{im(\phi_p + \phi_{q'})} e^{i2\pi kz_p} \text{sinc}(2\pi kz_{q'}) \frac{w^2(k)}{I_m'(|2\pi ka|) K_m'(|2\pi ka|)}$$

$$M_{33}(q, q') = \sum_{m=-\infty}^{+\infty} \int_{-\infty}^{+\infty} dk \Gamma_q^m(k) c_{q'}^m(k) = \left(\frac{4\pi I}{\mu_o a^2} z_q^2\right) \sum_{m=-\infty}^{+\infty} \int_{-\infty}^{+\infty} dk e^{im(\phi_q + \phi_{q'})} \text{sinc}^2(2\pi kz_q) \frac{w^2(k)}{I_m'(|2\pi ka|) K_m'(|2\pi ka|)}$$

the values of the azimuthal current density over a set of coordinates:

$$J_\phi(\phi_p, z_p) = J_{\phi p}; \quad p = 1{:}P \qquad [18]$$

Azimuthal current constraints of this form have been introduced previously (21); however, it should be noted that only the use of both the above forms of current constraint (closure and point azimuthal constraints) provides a sufficient and necessary condition for current density to be zero beyond $\pm z_q$. The closure constraint alone does not disallow closed current loops outside the bounded region whereas constraining the azimuthal current density to be zero does not prohibit non-zero longitudinal current density, $J_z(\phi, z)$ at the P constraint points; this will be made clear by example in the Results section.

Mathematically the current constraints represent a simple extension of the minimum inductance method outlined above. Both the closure constraint and the P current constraints must first be expressed as functions of $j_\phi^m(k)$:

$$\Lambda(\phi_q, z_q)$$

$$[19a]$$

$$= (2z_q) \sum_{m=-\infty}^{+\infty} \int_{-\infty}^{+\infty} dk e^{im\phi_q} \text{sinc}(2\pi kz_q) j_\phi^m(k)$$

$$J_\phi(\phi_p, z_p) = \sum_{m=-\infty}^{+\infty} \int_{-\infty}^{+\infty} dk e^{im\phi_p} e^{i2\pi kz_p} j_\phi^m(k) \qquad [19b]$$

With the constraint equations written as above, the functional to be optimized would take a form similar to

Eq. [11] and the optimal $j_\phi^m(k)$ obtained as before; however, there is a practical issue involved in the constraint of current that gives reason to alter Eq. [19]. The prescription of $J_\phi(\phi, z)$ at a finite set of points does not prevent large values of $J_\phi(\phi, z)$ between the constraint points. As the current constraints are moved closer together (requiring a larger number of constraints to cover the same area) non-zero interconstraint $J_\phi(\phi, z)$ values correspond to increasing power at high spatial frequencies, i.e., at high k values in $j_\phi^m(k)$. Although there is no theoretical limitation on the spatial frequency content of $J_\phi(\phi, z)$, any practical design will involve a maximum tolerable spatial frequency. The particular frequency will depend on the application and will often be determined by both the width and minimum bending radius of the conductor to be used in the final winding of the coil. For these reasons we filter out the impractically high frequency components of $J_\phi(\phi, z)$ via an apodizing function $w(k)$:

$$J_\phi(\phi, z) = \sum_{m=-\infty}^{+\infty} \int_{-\infty}^{+\infty} dk e^{im\phi} e^{i2\pi kz} w(k) j_\phi^m(k) \qquad [20]$$

where in the present work, we have used the following functional form for $w(k)$:

$$w(k) = 1, \quad |k| < k_t$$

$$= \frac{1}{2}\left[1 + \cos\left(\pi \cdot \frac{|k| - k_t}{k_c - k_t}\right)\right], \quad k_t \le |k| < k_c \qquad [21]$$

$$= 0, \quad |k| \ge k_c$$

with k_t ("transition frequency") and k_c ("cutoff frequency") chosen based on the desired complexity of the final current density. To prevent changes in the direction of $J_\phi(\phi, z)$ from occurring on a scale smaller than Δz (for example, Δz could be set equal to twice the minimum turning radius of the wire to be used in coil construction), k_c should be set equal to $1/(2*\Delta z)$; k_t is then set to allow a smooth transition in $w(k)$ while preventing the attenuation of frequency components below k_t. It should be noted that the spacing of the current constraints is set equal to $1/(2*k_c)$ to prevent non-zero values of current density between constraint positions. Examples of specific transition and cutoff frequency values used in practical designs will be given in the Results section. We now apply the closure and current constraints to $J_\phi(\phi, z)$ given above:

$$\Lambda(\phi_q, z_q) = \sum_{m=-\infty}^{+\infty} \int_{-\infty}^{+\infty} dk \Gamma_q^m(k) j_\phi^m(k) \quad [22]$$

$$\Gamma_q^m(k) = (2z_q)e^{im\phi_q}\text{sinc}(2\pi k z_q)w(k) \quad [23]$$

and

$$J_\phi(\phi_p, z_p) = \sum_{m=-\infty}^{+\infty} \int_{-\infty}^{+\infty} dk \Phi_p^m(k) j_\phi^m(k) \quad [24]$$

$$\Phi_p^m(k) = e^{im\phi_p}e^{i2\pi k z_p}w(k) \quad [25]$$

The apodizing function $w(k)$ must also be incorporated into the B_z constraint expressions to assure that the field constraints will be met by the constructed current density:

$$B_z(r_n, \phi_n, z_n) = \sum_{m=-\infty}^{+\infty} \int_{-\infty}^{+\infty} dk \Psi_n^m(k) j_\phi^m(k) \quad [26]$$

$$\Psi_n^m(k) = (-\mu_o a)e^{im\phi_n}e^{i2\pi k z_n}|k|I_m(|2\pi k r_n|)$$
$$\cdot K_m'(|2\pi k a|)w(k) \quad [27]$$

Only the three sets of constraint equations are modified with the inclusion of $w(k)$; the inductance expression of Eq. [12] does not require apodization. The integrand of Eq. [12] naturally attenuates high spatial frequencies more extremely than $w(k)$ and therefore its inclusion is unnecessary. The attenuating property of the inductance integrand can be seen by noting that for large k, $I_m(k) \sim e^k/(\sqrt{2\pi k})$, $K_m(k) \sim e^{-k}/(\sqrt{2\pi k})$, and therefore the product is approximately $1/k$.

With the apodization discussed above, the functional to be minimized takes the form:

$$U\{j_\phi^m(k)\} = L\{j_\phi^m(k)\} + \sum_{n=1}^{N} \lambda_n[B_z(r_n, \phi_n, z_n) - B_{zn}]$$
$$\quad [28]$$
$$+ \sum_{p=1}^{P} \lambda_p[J_\phi(\phi_p, z_p) - J_{\phi p}] + \lambda_q[\Lambda(\phi_q, z_q) - \Lambda_q]$$

where the inductance expression is given by Eq. [12] and the summation over all constraints is that of Eq. [11] with $N+P+1$ constraints based on Eqs. [22], [24], and [26]. Taking the derivative of $U\{j_\phi^m(k)\}$ with respect to $j_\phi^m(k)$, setting the result equal to zero, and solving for $j_\phi^m(k)$, we get:

$$j_\phi^m(k) = \sum_{n=1}^{N} \lambda_n a_n^m(k) + \sum_{p=1}^{P} \lambda_p b_p^m(k) + \lambda_q c_q^m(k) \quad [29]$$

where

$$a_n^m(k) = \left(\frac{-\pi}{a}\right)e^{im\phi_n}e^{i2\pi k z_n}|k| \frac{I_m(|2\pi k r_n|)}{I_m'(|2\pi k a|)} w(k) \quad [30]$$

$$b_p^m(k) = \left(\frac{\pi}{\mu_o a^2}\right)e^{im\phi_p}e^{i2\pi k z_p} \frac{w(k)}{I_m'(|2\pi k a|) K_m'(|2\pi k a|)} \quad [31]$$

$$c_q^m(k) = \left(\frac{2\pi z_q}{\mu_o a^2}\right)e^{im\phi_q}\text{sinc}(2\pi k z_q)$$
$$\quad [32]$$
$$\cdot \frac{w(k)}{I_m'(|2\pi k a|) K_m'(|2\pi k a|)}$$

The set of $\{\lambda_n, \lambda_p, \lambda_q\}$ (representing $N+P+1$ total unknowns) is found by substituting $j_\phi^m(k)$ expressed by Eq. [29] into the $N+P+1$ constraint Eqs. [22], [24], and [26] to get the following:

$$B_{zn} = \sum_{m=-\infty}^{+\infty} \int_{-\infty}^{+\infty} dk \Psi_n^m(k) \left[\sum_{n'=1}^{N} \lambda_{n'} a_{n'}^m(k) \right.$$
$$\quad [33]$$
$$\left. + \sum_{p'=1}^{P} \lambda_{p'} b_{p'}^m(k) + \lambda_{q'} c_q^m(k) \right]$$

$$J_{\phi p} = \sum_{m=-\infty}^{+\infty} \int_{-\infty}^{+\infty} dk \Phi_p^m(k) \left[\sum_{n'=1}^{N} \lambda_{n'} a_{n'}^m(k) \right.$$
$$\quad [34]$$
$$\left. + \sum_{p'=1}^{P} \lambda_{p'} b_{p'}^m(k) + \lambda_{q'} c_q^m(k) \right]$$

$$\Lambda_q = \sum_{m=-\infty}^{+\infty} \int_{-\infty}^{+\infty} dk \Gamma_q^m(k) \left[\sum_{n'=1}^{N} \lambda_{n'} a_{n'}^m(k) \right.$$
$$\quad [35]$$
$$\left. + \sum_{p'=1}^{P} \lambda_{p'} b_{p'}^m(k) + \lambda_{q'} c_q^m(k) \right]$$

This set of equations can be written as a single matrix equation, the solution of which is a vector of the required Lagrange multipliers:

$$\mathbf{M}\underline{\lambda} = \underline{\mathbf{c}} \quad [36]$$

In block form Eq. [36] is:

$$\begin{bmatrix} \mathbf{M_{11}} & \mathbf{M_{12}} & \mathbf{M_{13}} \\ \mathbf{M_{12}^T} & \mathbf{M_{22}} & \mathbf{M_{23}} \\ \mathbf{M_{13}^T} & \mathbf{M_{23}^T} & \mathbf{M_{33}} \end{bmatrix} \begin{bmatrix} \lambda_N \\ \lambda_P \\ \lambda_Q \end{bmatrix} = \begin{bmatrix} \mathbf{B_{zN}} \\ \mathbf{J_{\phi P}} \\ \Lambda_Q \end{bmatrix} \quad [37]$$

where the six distinct blocks of the matrix are all known functions of the constraint coordinates and are listed in Table 1. The $\mathbf{M_{11}}$ block is identical to that used in Eq. [16] but derived using $a_n^m(k)$ given by Eq. [30] instead of Eq. [15], and the elements are functions of the field constraint coordinates only. If the azimuthal current constraints are included, the resulting $N+P$ by $N+P$ matrix is composed of $\mathbf{M_{11}}$, $\mathbf{M_{12}}$, and $\mathbf{M_{22}}$; here $\mathbf{M_{22}}$ is only a function of the current constraint coordinates whereas $\mathbf{M_{12}}$ is a function of both the field and current coordinates. The inclusion of the closure constraint increases the dimension of the matrix by 1 (now of rank $N+P+1$) and $\mathbf{M_{33}}$ depends only on the closure coordinates. The $\mathbf{M_{23}}$ block includes both closure and current coordinates while $\mathbf{M_{13}}$ has both closure and field coordinates. The Lagrange multiplier vector would be $\{\lambda_n\}$ for only field constraints, $\{\lambda_n, \lambda_p\}$ for field and current, $\{\lambda_n, \lambda_q\}$ for field and closure, and $\{\lambda_n, \lambda_p, \lambda_q\}$ for all three types of constraints. The constant vector on the right hand side of Eq. [37] is partitioned in an analogous way.

With the above mathematical forms in place, the design algorithm is simply the following. First a set of constraints is chosen that will assure that the gradient coil will fall within specifications. The field constraints determine the type of gradient coil (transverse versus longitudinal), the gradient strength, and the size and absolute placement of the region of uniformity. Current and closure constraints are chosen such that the physical coil will be of the required size and the region of gradient uniformity is positioned as desired relative to the current density. Once all constraints are set, the elements of matrix $\mathbf{M}$ are computed via the known forms in Table 1 and the constraint vector is assembled. Equation [37] is solved for the Lagrange multipliers through Gaussian elimination or an alternative technique. The multipliers are used in Eq. [29] to yield $j_\phi^m(k)$, the transform of which gives the current density of minimum inductance satisfying all of the specified design constraints.

RESULTS AND DISCUSSION

The theory in the previous section has been implemented in the MATLAB software language (version 4.2, The Mathworks Inc., Natick, MA) and used to create a variety of gradient coil designs, representative examples of which are presented in the following paragraphs. The azimuthal current density, $J_\phi(\phi, z)$, is the final result of the above analysis; however, the discrete wire pattern approximating the current density is obtained via stream function methods described elsewhere (7). The entire calculation, from specification of all constraints to determination of $J_\phi(\phi, z)$ and the approximation with discrete wire paths, typically takes less than three minutes on a Sun Microsystems ULTRA SPARC 1/140 workstation. All analytic forms involved in the evaluation of the matrix elements of Table 1 and subsequent construction of $J_\phi(\phi, z)$ are well known (exponential and modified Bessel functions) and there are readily available and accurate routines within the MATLAB package for their evaluation. Once the final wire pattern is obtained, the pattern for the entire coil is discretized into on the order of 10,000 to 20,000 elements, allowing for numerical verification of the achieved magnetic fields and inductance using the Biot-Savart equation and Neumann's formula (22), respectively. Gradient efficiency (η, defined as gradient strength per unit current) can be gained at the cost of increasing coil inductance simply by increasing the number of wires used to sample the current density. Efficiency varies linearly with wire number while the inductance increases as the square of the wire number. Inductance also varies as the fifth power of coil radius (for constant efficiency and wire pattern (16)); therefore, for a given design, $\eta \cdot a^{2.5}/(\sqrt{L})$ is a constant, independent of both radius and wire number. We use this quantity as a figure-of-merit or performance measure in comparing different designs.

The most familiar gradient coil application is the establishment of a uniform gradient field within the central region of a current carrying cylinder. To demonstrate the effectiveness of the combination of closure and current constraints in limiting the extent of the final current density, the four different combinations of constraints described in the theory section: field, field and closure, field and current, and field, closure, and current, were applied to the problem of designing an extremely short aspect ratio (1:1, coil length:coil diameter) central region of interest (ROI) coil. Field constraints must always be included because the minimum inductance current density not constrained to produce any field is simply zero everywhere. It has been suggested in the literature (5) that such extremely short coil designs are not possible with target field methods; this example serves to demonstrate that using the methods developed in this paper, very short aspect ratio coils can be designed in a straightforward manner. An ROI of length $0.75*a$ was chosen over which four field constraints were placed: $r_n = a/4$, $\phi_n = 0$, $z_n = \{-3, -1, 1, 3\}*(a/8)$ with $B_{zn} = G_x*r_n$ where G_x is the transverse gradient strength in T/m. The design corresponding to those specifications is shown in Figs. 1a and 1b. The coil has an aspect ratio of over 2.5:1 with the edge of the ROI located more than $2a$ away from the edge of the coil. To limit the aspect ratio to 1:1 while maintaining the size of the central ROI, a closure constraint was placed at the desired position (z_q) and a series of current constraints placed over the adjacent region; specifically, the closure constraint was $\Lambda = 0$ for $\phi_q = 0$, $z_q = a$ and the current constraints were $J_{\phi p} = 0$ at $\phi_p = 0$, $z_p = \pm\{(z_q + dz*i); \text{ for } i = 0:55 \text{ and } dz = (3a/55)\}$. The apodization function, $w(k)$, was of the form given in Eq. [21] with $k_c = 1/(2*dz)$ and $k_t = 0.6*k_c$, set to prevent non-zero $J_\phi(\phi, z)$ between constraint points. This constitutes 117 constraints in total ($N = 4$, $P = 2*56 = 112$, $Q = 1$) and the results are shown in Figs. 1c–1h. The effects of the closure and current constraints applied separately are shown in Figs. 1c–1d and 1e–1f, respectively. Figures 1c–1h demonstrate that the combination of closure and current constraints is a sufficient condition for the con-
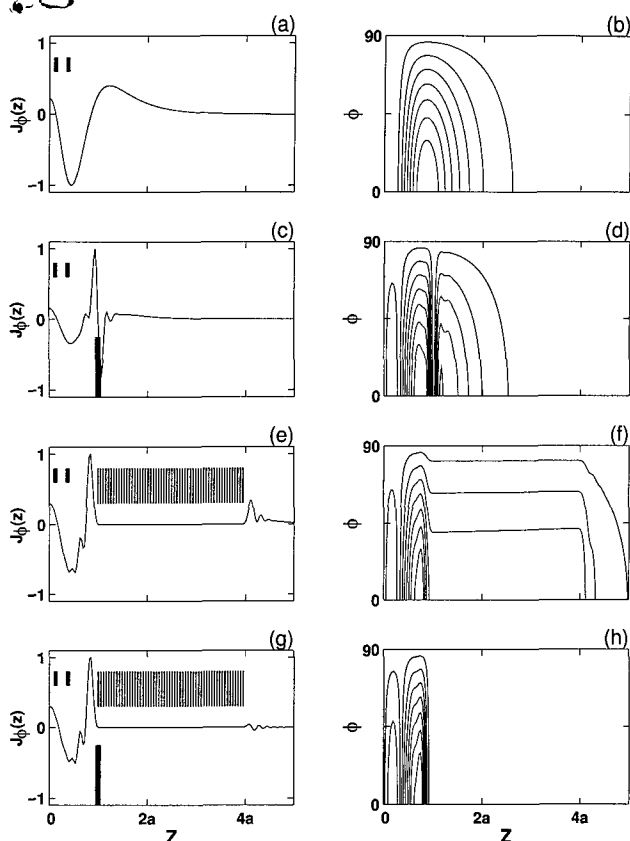
FIG. 1. Middle ROI, normalized $J_\phi(z)$s with corresponding half-quadrant wire paths for: (a–b) field constraints only (short heavy bars); (c–d) field and closure (long heavy bar) constraints; (e–f) field and current (long bars); (g–h) field, current, and closure constraints. All constraints are placed symmetrically about $z = 0$.

straint of gradient coil length and they must be used together to be effective in that regard. The calculated gradient efficiencies and inductances for the respective designs are shown in Table 2 for $a = 0.325$ m (approximate radius for a full body gradient coil). As expected, the merit figure and the aspect ratio decrease as constraints are added; however, access to the usable region is significantly improved. For the 1:1 design, the region of 20% gradient deviation extends over a cylinder of diam-

Table 2
Gradient Design Example Results Summary

	Coil Parameters		
	Efficiency [mT/m/A]	Inductance [μH]	Merit [*10⁻⁵]ᵃ
Central ROI designsᵇ			
Field constraints	0.090	540	28
Field + closure constraints	0.074	604	22
Field + current constraints	0.070	656	20
Field + closure + current	0.055	690	15
Edge ROI designsᵇ			
Field constraints	0.061	465	17
Field + closure constraints	0.057	460	16
Field + current constraints	0.053	520	14
Field + closure + current	0.032	290	11

ᵃ Merit = $(\eta * a^{2.5})/L^{1/2}$ in S.I. units.
ᵇ Both design sets are for $a = 0.325$ m.

eter 0.20 m and length 0.30 m at the coil center, beginning 0.20 m from the coil edge, whereas for the 2.5:1 design, the same region extends over a cylinder of diameter 0.30 m and length 0.40 m at the coil center, beginning 0.75 m from the coil edge. Figure 2a shows calculated contours of 20% gradient deviation on the xz plane for both the 2.5:1 and 1:1 aspect ratio designs. It can be seen that the uniformity of the gradient field is not compromised in a major way through the addition of the current constraints. The wire pattern for the 1:1 design is only slightly more complex than the 2.5:1 design, the only potential concern is the increased current density at the coil edge. This increased density is common to constrained length gradient coil designs, and is typically only two to three times the maximum density of the pure minimum inductance designs. Increasing the aspect ratio results in a decreased current density at the coil edge and the two can be traded off against each other in a controlled manner.

As the above example suggests, the ability to restrict current density to a specified region of the coil allows for the control of the position of the ROI with respect to the physical end of the coil; an important extension of this idea is the design of gradient coils with a usable region of uniformity arbitrarily close to the end of the coil. To design such an edge gradient coil, a set of field constraints was placed over the edge ROI just as was done in the design described above. A second set of field constraints was placed at the opposite end of the coil, forcing the first moment of the current density to be zero by symmetry, thereby guaranteeing a torque balanced coil
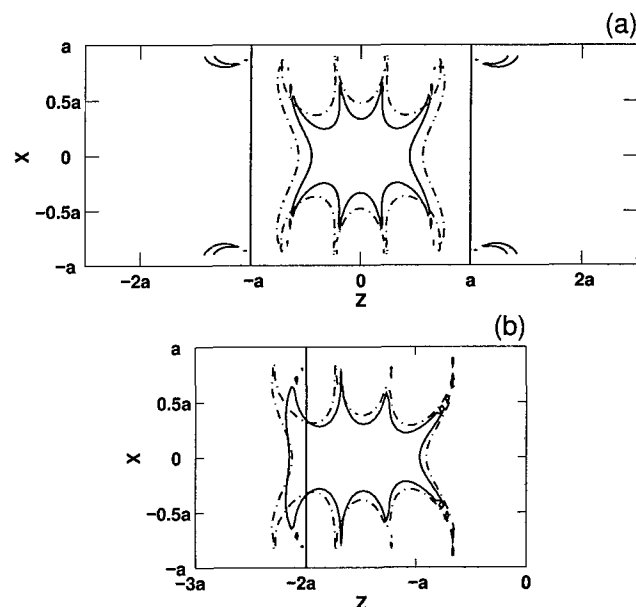

FIG. 2. Contour plots of 20% deviation from uniformity over xz planes for designs with and without current constraints. (a) shows 20% contours for the central ROI designs with (solid line) and without (dotted line) current constraints. The solid vertical line indicates the physical edge of the coil for the 1:1 aspect ratio design. (b) shows 20% contours over one half of the xz plane for the edge ROI designs with (solid line) and without (dotted line) current constraints. The vertical line indicates the position of the physical edge of the coil for the current constrained design.
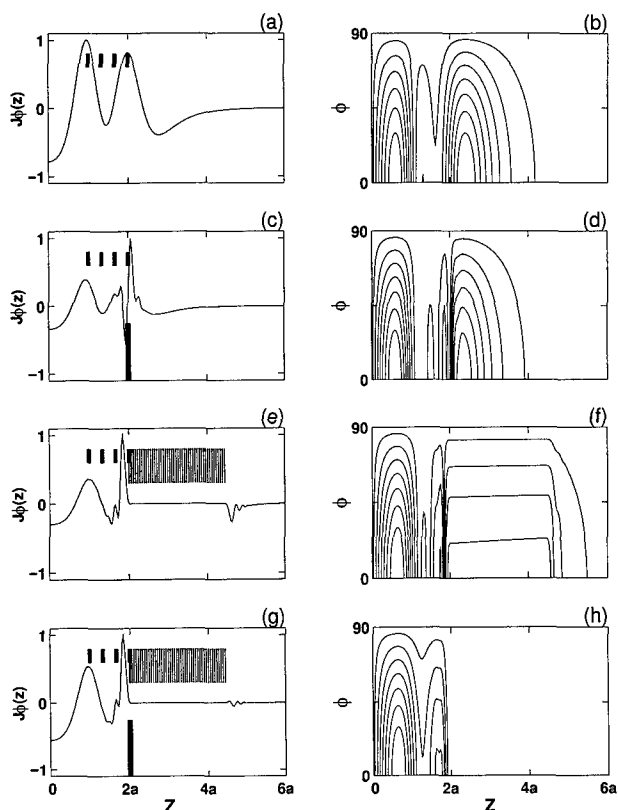
FIG. 3. Edge ROI, normalized $J_\phi(z)$s with corresponding half-quadrant wire paths for: (a–b) field constraints only (short heavy bars); (c–d) field and closure (long heavy bar) constraints; (e–f) field and current (long bars); (g–h) field, current, and closure constraints. All constraints are placed symmetrically about z = 0. Note relative position of closure, current, and field constraints yielding the edge gradient coil.

[20]. No field constraints were specified over the central region because that area will not be utilized and unnecessary constraints only serve to increase the inductance of the design. The end of the coil was moved adjacent to the ROI by applying closure at the outer edges of the field constraint sets and a set of current constraints applied over the region exterior to the closure positions. As an example, four field constraints were placed over a region extending from $z = a$ to $z = 2a$: $r_n = a/4$, $\phi_n = 0$, $z_n = \{a + (a/3)*i\}$, where $i = 0{:}3$ with $B_{zn} = G_x \cdot r_n$. The same set was placed over the corresponding region on the negative side of the coil, constituting eight field constraints in total. The minimum inductance design subject to these field constraints is shown in Figs. 3a and 3b. The aspect ratio of the design is more than 4:1 and the outer edge of the ROI is more than $2a$ away from the edge of the coil. The addition of the closure constraint at $\phi_q = 0$, $z_q = \max(z_n) = 2a$, and the set of current constraints: $J_{\phi p} = 0$ at $\phi_p = 0$, $z_p = \pm\{(z_q + dz*i)$; for $i = 0{:}45$ and $dz = (2a/45)\}$, constitutes 101 constraints in total ($N = 8$, $P = 2*46 = 92$, $Q = 1$) and as in the central ROI design example, $w(k)$ was as shown in Eq. [21] with $k_c = 1/(2*dz)$ and $k_t = 0.6*k_c$; this results in the edge gradient coil design shown in Figs. 3g and 3h. For $a = 0.325$ m (approximate body coil dimension) the region of 20% gradient uniformity begins 7 cm *outside* the edge of the

coil and ends 32 cm inside. For comparison, Figs. 3c–3f show the results of applying the closure and current constraints separately. The calculated gradient efficiencies and inductances are listed in Table 2. Figure 2b shows the calculated contours of 20% gradient deviation on the *xz* plane for designs with and without the above current constraints; again, it can be seen that the current constraints do not significantly affect the achieved gradient homogeneity. The edge coil wire pattern is not significantly more complicated than the unconstrained version of Fig. 3b nor is the maximum current density (located at the end of the coil) extreme, being slightly more than twice its maximum value in the unconstrained example. Just as in the 1:1 central ROI design example, the positioning of the ROI at the coil edge is accompanied by a decrease in the merit figure. The achieved merit figure depends on the size and position of the specified ROI with respect to the allowed extent of the current density. These can be traded off against each other for any particular application.

The ability to constrain the position of the imaging region with respect to the physical gradient coil with target field methods should represent an important improvement in gradient coil design in general. The minimum inductance target field method already developed possesses the advantage that it is an inverse solution to the design problem. It is a very numerically efficient technique that takes advantage of the FFT algorithm [23] and its use allows the designer to gain an understanding of the connection between spatial frequency components of the magnetic field and current density. We believe that one of the major limitations of target field methods has been the lack of direct control over the nature of the final form of the current density. The theory described in this paper removes this limitation. There are several important applications of this method. The constraint of total coil length for a middle ROI coil will allow the optimal design of gradients for use with short-bore magnets. It is also useful to limit gradient coil lengths simply for ease of construction and potential reduction of associated costs. Head sized gradient coil design will especially benefit from this method. The positioning of the ROI directly adjacent to the coil edge will allow, for the first time, imaging of the neck region with a head-sized gradient coil. It should also allow the imaging of the brain region with the subject's eyes positioned at or outside the coil edge. This would be useful in functional imaging studies where visual communication with the subject is necessary. We have designed a head-sized gradient coil capable of imaging with efficiencies of 0.4 mT/m/A over a region adjacent to the coil edge and having an inductance of 800 μH; we will report on the details of this design and experimental results of imaging with this coil in a forthcoming paper. The ability to easily design gradients of this nature should make possible new imaging methods that were previously considered impractical.

REFERENCES

1. E. Wong, A. Jesmanowicz, J. S. Hyde, Coil optimization for MRI by conjugate gradient descent. *Magn. Reson. Med.* **21**, 39–48 (1991).
2. E. R. Andrew, E. Szczesniak, Low inductance transverse gradient

system of restricted length. *Magn. Reson. Imaging* **13**, 607–613 (1995).

3. S. Crozier, D. M. Doddrell, Gradient-coil design by simulated annealing. *J. Magn. Reson.* **103**, 354–357 (1993).

4. S. Crozier, L. K. Forbes, D. M. Doddrell, The design of transverse gradient coils of restricted length by simulated annealing. *J. Magn. Reson. A.* **107**, 126–128 (1994).

5. S. Crozier, D. M. Doddrell, A design methodology for short, whole-body, shielded gradient coils for MRI. *Magn. Reson. Imaging* **13**, 615–620 (1995).

6. M. L. Buszko, M. F. Kempka, E. Szczesniak, D. C. Wang, E. R. Andrew, Optimization of transverse gradient coils with coaxial return paths by simulated annealing. *J. Magn. Reson. B.* **112**, 207–213 (1996).

7. W. A. Edelstein, J. F. Schenck, Current streamline method for coil construction. US Patent 4,840,700; priority date July 13, 1987.

8. K. Yoda, Analytic design method of self-shielded planar coils. *J. Appl. Phys.* **67**, 4349–4353 (1990).

9. M. A. Martens, L. S. Petropoulos, R. W. Brown, J. H. Andrews, M. A. Morich, J. L. Patrick, Insertable biplanar gradient coil for MR imaging. *Rev. Sci. Instrum.* **62**, 2639–2645 (1991).

10. R. Turner, A target field approach to optimal coil design. *J. Phys. D.* **19**, L147–151 (1986).

11. T. W. Carlson, K. A. Derby, K. C. Haveryszko, M. Weideman, Design and evaluation of shielded gradient coils. *Magn. Reson. Med.* **26**, 191–206 (1992).

12. H. Liu, L. S. Petropoulos, A spherical gradient coil for ultrafast imaging applications, *in* "Proc., ISMRM, 4th Annual Meeting, New York, 1996," p. 1394.

13. Q. Liu, D. G. Hughes, P. S. Allen, Improved, minimum-inductance, elliptic-cylinder z-gradient coil using axial and azimuthal current flow. *J. Magn. Reson. B.* **113**, 228–235 (1996).

14. J. W. Carlson, M. S. Roos, Shielded gradient coils on hyperbolic surfaces of revolution. *Magn. Reson. Med.* **34**, 762–769 (1995).

15. C. D. Eccles, S. Crozier, W. Roffman, D. M. Doddrell, P. Back, P. T. Callaghan, Practical aspects of shielded gradient-coil design for localized in vivo NMR spectroscopy and small-scale imaging. *Magn. Reson. Imaging* **12**, 621–630 (1994).

16. R. Turner, Gradient coil design: a review of methods. *Magn. Reson. Imaging* **11**, 903–920 (1993).

17. R. Turner, Minimum inductance coils. *J. Phys. E.* **21**, 948–952 (1988).

18. J. D. Jackson, "Classical Electrodynamics," Wiley, New York, 1962.

19. F. B. Hildebrand, "Advanced Calculus for Applications," 2nd ed., Prentice-Hall, NJ, 1976.

20. D. C. Alsop, T. J. Connick, Optimization of torque-balanced asymmetric head gradient coils. *Magn. Reson. Med.* **35**, 875–886 (1996).

21. R. Turner, Electrical coils. US Patent 5,289,151; priority date February 22, 1994.

22. J. R. Reitz, F. J. Milford, R. W. Christy, "Foundations of Electromagnetic Theory," 4th ed., Addison-Wesley, New York, 1989.

23. J. W. Cooley, J. W. Tukey, An algorithm for the machine computation of complex Fourier series. *Math. Comput.* **19**, 297–301 (1965).

DEPARTMENT OF THE ARMY
US ARMY MEDICAL RESEARCH AND MATERIEL COMMAND
504 SCOTT STREET
FORT DETRICK, MARYLAND 21702-5012

REPLY TO
ATTENTION OF:

MCMR-RMI-S   (70-1y)   26 Aug 02

MEMORANDUM FOR Administrator, Defense Technical Information
Center (DTIC-OCA), 8725 John J. Kingman Road, Fort Belvoir,
VA 22060-6218

SUBJECT: Request Change in Distribution Statement

1.   The U.S. Army Medical Research and Materiel Command has
reexamined the need for the limitation assigned to technical
reports written for this Command. Request the limited
distribution statement for the enclosed accession numbers be
changed to "Approved for public release; distribution unlimited."
These reports should be released to the National Technical
Information Service.

2.   Point of contact for this request is Ms. Kristin Morrow at
DSN 343-7327 or by e-mail at Kristin.Morrow@det.amedd.army.mil.

FOR THE COMMANDER:

Encl   PHYLIS M. RINEHART
                                  Deputy Chief of Staff for
                                     Information Management

ADB274369
ADB256383
ADB264003
ADB274462
ADB266221
ADB274470
ADB266221
ADB274464
ADB259044
ADB258808
ADB266026
ADB274658
ADB258831
ADB266077
ADB274348
ADB274273
ADB258193
ADB274516
ADB259018
ADB231912
ADB244626
ADB256677
ADB229447
ADB240218
ADB258619
ADB259398
ADB275140
ADB240473
ADB254579
ADB277040
ADB249647
ADB275184
ADB259035
ADB244774
ADB258195
ADB244675
ADB257208
ADB267108
ADB244889
ADB257384
ADB270660
ADB274493
ADB261527
ADB274286
ADB274269
ADB274592
ADB274604

ADB274596
ADB258952
ADB265976
ADB274350
ADB274346
ADB257408
ADB274474
ADB260285
ADB274568
ADB266076
ADB274441
ADB253499
ADB274406
ADB262090
ADB261103
ADB274372